

Dynamic Fault Interaction during a Fluid-Injection-Induced Earthquake: The 2017 M_w 5.5 Pohang Event

Kadek Hendrawan Palgunadi^{*1}, Alice-Agnes Gabriel², Thomas Ulrich², José Ángel López-Comino^{1,3,4,5}, and Paul Martin Mai¹

ABSTRACT

The 15 November 2017 M_w 5.5 Pohang, South Korea, earthquake has been linked to hydraulic stimulation and fluid injections, making it the largest induced seismic event associated with an enhanced geothermal system. To understand its source dynamics and fault interactions, we conduct the first 3D high-resolution spontaneous dynamic rupture simulations of an induced earthquake. We account for topography, off-fault plastic deformation under depth-dependent bulk cohesion, rapid velocity weakening friction, and 1D subsurface structure. A guided fault reconstruction approach that clusters spatiotemporal aftershock locations (including their uncertainties) is used to identify a main and a secondary fault plane that intersect under a shallow angle of 15°. Based on simple Mohr–Coulomb failure analysis and 180 dynamic rupture experiments in which we vary local stress loading conditions, fluid pressure, and relative fault strength, we identify a preferred two-fault-plane scenario that well reproduces observations. We find that the regional far-field tectonic stress regime promotes pure strike-slip faulting, whereas local stress conditions constrained by borehole logging generate the observed thrust-faulting component. Our preferred model is characterized by overpressurized pore fluids, nonoptimally oriented but dynamically weak faults and a close-to-critical local stress state. In our model, earthquake rupture “jumps” to the secondary fault by dynamic triggering, generating a measurable non-double-couple component. Our simulations suggest that complex dynamic fault interaction may occur during fluid-injection-induced earthquakes and that local stress perturbations dominate over regional stress conditions. Therefore, our findings have important implications for seismic hazard in active georeservoir.

depth dependent bulk cohesion?
rapid velocity weakening friction?

what should optimal orientation be like?
what is Close-to-critical local stress state

Plain sum:

1. [fault reconstruction] aftershocks locations > main and secondary fault plane have an angle of 15 degree;
2. Preferred model > overpressurized pore fluids, nonoptimally oriented, dynamically weak faults, CtC local stress state.
3. local stress perturbations dominate over regional stress conditions

KEY POINTS

- We conduct 3D high-resolution spontaneous dynamic rupture simulations of an induced earthquake.
- Local stress conditions, dynamically weak and critically stressed faults are responsible for spontaneous rupture.
- Physics-based approaches could be combined with near-field seismic monitoring in georeservoir.

Supplemental Material

Gyeongju earthquake. The Pohang earthquake caused one fatality, injured 82 people, and generated more than \$300 million U.S. in total economic loss (Ellsworth *et al.*, 2019; Lee *et al.*, 2019). The hypocenter was located approximately 10 km northeast of Pohang city, close to the Pohang enhanced geothermal system (EGS) site (36.106° N, 129.373° E, and depth ~4.27 km, Korean Government Commission, 2019). Its proximity to the EGS site and hypocentral depth similar to the open-hole sections of the fluid-injection wells (Fig. 1) quickly raised questions if this

1. Physical Science and Engineering, King Abdullah University of Science and Technology, Thuwal, Saudi Arabia; 2. Department of Earth and Environmental Sciences, Geophysics, Ludwig-Maximilians-Universität München, Munich, Germany; 3. Institute of Geosciences University of Potsdam, Potsdam-Golm, Germany; 4. Instituto Andaluz de Geofísica, Universidad de Granada, Spain; 5. Departamento de Física Teórica y del Cosmos, Universidad de Granada, Spain

*Corresponding author: kadek.palgunadi@kaust.edu.sa

Cite this article as Palgunadi, K. H., A.-A. Gabriel, T. Ulrich, J. Á. López-Comino, and P. M. Mai (2020). Dynamic Fault Interaction during a Fluid-Injection-Induced Earthquake: The 2017 M_w 5.5 Pohang Event, *Bull. Seismol. Soc. Am.* **XX**, 1–22, doi: 10.1785/0120200106

© Seismological Society of America

INTRODUCTION

The Korean Peninsula is known to have a rather low level of seismicity (compared with neighboring countries such as China and Japan), because it lies on the continental margin of the east Eurasian plate. However, on 15 November 2017 (05:29:31 UTC), a magnitude M_w 5.5 earthquake occurred (hereinafter, the Pohang earthquake), the second-largest recorded earthquake in South Korea following the 2016 M_L 5.8

Earthquake linked to fluid injection > [180 experiments] vary fluid pressure> preferred model is overpressurized pore fluids dynamically weak faults

Can we generalize this procedure to 2017 Botswana earthquake?

local stress conditions; dynamically weak and critically stressed faults > spontaneous rupture

what are local stress conditions?

what is critical stressed faults?

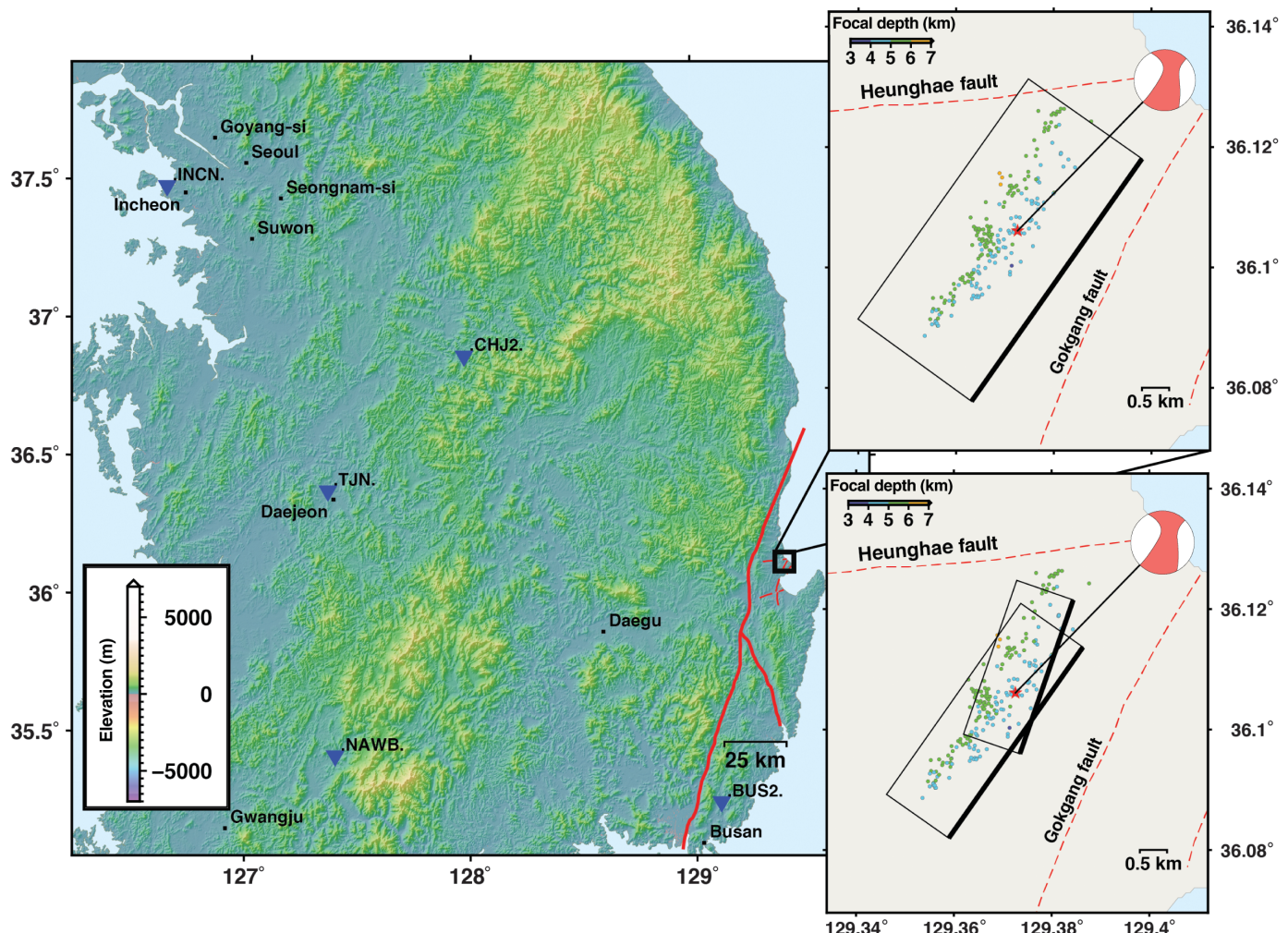
Introduction:

1. the hypercenter close to the geothermal site, and ~4.27 km in depth

2. Proximity of the EGS site; hypocentral depth \approx fluid-injection wells \Rightarrow earthquake is caused by EGS activities

complex dynamic fault interaction may occur during fluid-injection-induced earthquakes and that local stress perturbations dominate over regional stress conditions

How do we account for topography, off-fault plastic deformation under depth-dependent bulk cohesion, rapid velocity weakening friction, and 1D subsurface structure?



earthquake is associated with EGS activities (Grigoli *et al.*, 2018; Kim *et al.*, 2018).

The Pohang EGS project was designed to create an enhanced geothermal reservoir within a low permeability crystalline basement. The basement is overlain by cretaceous volcanic and sedimentary rocks, tertiary volcanic and sedimentary rocks, and quaternary sediments (Ellsworth *et al.*, 2019; Korean Government Commission, 2019). During a period of 4 yr (2012–2016), two geothermal wells (maximum depth ~4.3 km) were drilled for hydraulic stimulations. At the surface, both wells are separated by only 6 m distance, increasing to a separation of 599 m at a depth of ~4.3 km. For well PX-1, the drilling was stuck at a depth of 2419 m, and hence sidetracked into west-northwest direction. Well PX-2 experienced large mud loss in the depth interval 3830–3840 m, whereas cuttings contain significant fractions of friable round-shaped mud balls typical for fault gouge (Ellsworth *et al.*, 2019; Korean Government Commission, 2019). In these geothermal wells, five hydraulic stimulations were conducted between 29 January 2016 and 18 September 2018. During this period, each hydraulic stimulation phase was associated with seismicity. The magnitudes during and after stimulations reached up to

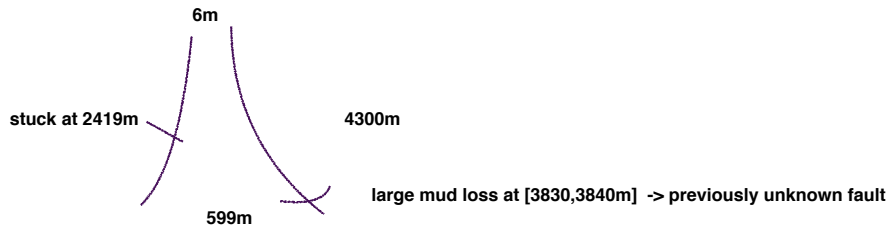
Figure 1. Map of the South Korean Peninsula showing the near-regional broadband stations (blue triangles). Solid and dashed lines represent the Yangsan and interpreted geological faults near the Pohang enhanced geothermal system (EGS) site, respectively. The two inset plots present the location and geometry of the faults of model 1F (upper panel) and model 2F (lower panel). Thicker black lines mark the near-surface edge of the fault planes. Colored dots depict aftershocks locations extracted from Kim *et al.* (2018). The non-double-couple solution of Grigoli *et al.* (2018) is also shown.

$M_L \approx 3$, whereas events were distributed within a restricted area close to the wells (Woo *et al.*, 2019). The depth of the seismicity before the Pohang earthquake spans the depth range 3.8–4.4 km, comparable with the open-hole section of the well at ~4.3 km depth (Ellsworth *et al.*, 2019).

Recent studies confirm that the Pohang earthquake was induced by hydraulic stimulation and extensive fluid injection at this EGS site (Ellsworth *et al.*, 2019; Korean Government Commission, 2019; Woo *et al.*, 2019; Kim *et al.*, 2020). These activities are considered to have activated the previously unmapped fault, which was found to intersect well PX-2 at a depth of ~3.8 km. Chang *et al.* (2020) point out that increased pore-pressure stressing due to multiple injection wells at the

EGS project: low permeability crystalline basement; overlain, volcanic and sedimentary rocks

An enhanced geothermal system (EGS) generates geothermal electricity without the need for natural convective hydrothermal resources. Until recently, geothermal power systems have exploited only resources where naturally occurring heat, water, and rock permeability are sufficient to allow energy extraction.



hydraulic stimulation phase - seismicity -> depth range [3.8, 4.4 km], M_L =3; close to the wells

1. Pohang earthquake was induced by hydraulic stimulation and extensive fluid injection at this EGS site
2. increased pore-pressure due to injection
3. the size of fluid-injection-induced earthquakes > pressure, location, and rate of fluid injection (Hofmann, 2019)
4. induced earthquakes are confined by a function of injected volume (McGarr, 2014; Galis et al., 2017).
5. in EGS reservoirs with extensive fluid injection and hydraulic stimulation, earthquakes with pronounced non-DC components may occur (Julian et al., 1998).
6. fluid injection > disturb the local stress state from the regional stress regime (Martínez-Garzón et al., 2013, 2014; Schoenball et al., 2014).

>

[investigate]

regional and local stress conditions

[act on]

>

different fault models

> a source mechanism with non-DC components

Pohang EGS site may have contributed to the mainshock generation. However, it has been argued that the size of fluid-injection-induced earthquakes can be controlled by managing pressure, location, and rate of fluid injection (Hofmann *et al.*, 2019). Data-driven empirical and numerical studies have shown that the induced earthquakes are confined by a function of injected volume (McGarr, 2014; Galis *et al.*, 2017).

two faults? Grigoli *et al.* (2018) find a complex-source mechanism for the Pohang earthquake with a significant non-double-couple (non-DC) component. They hypothesized that this earthquake involved failure on two different faults with slightly different focal mechanisms. In fact, in EGS reservoirs with extensive fluid injection and hydraulic stimulation, earthquakes with pronounced non-DC components may occur (Julian *et al.*, 1998). Moreover, fluid injections may induce local deviation of the stress state from the regional stress regime (Martínez-Garzón *et al.*, 2013, 2014; Schoenball *et al.*, 2014). Therefore, we examine how regional and local stress conditions acting on different fault models (single plane and two planes) determine the dynamic rupture process that leads to a source mechanism with non-DC components.

Dynamic rupture modeling aims to reproduce the physical processes that govern how earthquakes start, propagate, and stop for given stress and frictional conditions acting on fault surfaces. The earthquake dynamics are then a result of the model's initial conditions, such as geometry and frictional strength of the fault(s), the tectonic stress state, the regional lithological structure, and a frictional constitutive equation. Jin and Zoback (2018) model coseismic fully dynamic spontaneous fault rupture resulting from preseismic quasi-static loading exerted by fluid perturbations in a faulted porous medium in 2D. Duan (2016) models 2D dynamic rupture accounting for fluid effects of a propagating hydraulic fracture. Cappa and Rutqvist (2012) and Buijze *et al.* (2017) constrain the rupture onset in 2D dynamic rupture experiments by the stress state resulting from solving a coupled quasi-static poroelastic equation. Further 2D studies that model induced (not fully dynamic) earthquake rupture were linked to the diffusion equation, these studies include Garagash and Germanovich (2012), Richards-Dinger and Dieterich (2012), Viesca and Rice (2012), Dieterich *et al.* (2015), Galis *et al.* (2017), and Kroll *et al.* (2017). Using modern numerical methods and advanced hardware, very realistic 3D simulations represent explicitly the highly nonlinear dynamic rupture process (e.g., Heinecke *et al.*, 2014; Roten *et al.*, 2014; Uphoff *et al.*, 2017; Ulrich, Gabriel, Ampuero, and Xu, 2019; Ulrich, Vater, *et al.*, 2019; Wollherr *et al.*, 2019). The modeling results include spatial and temporal evolution of earthquake rupture, surface displacements, and ground shaking caused by the radiated seismic waves.

In this study, we investigate the dynamic rupture process under variable stress and fault-geometry assumptions for the Pohang earthquake, using the high-performance-computing enabled software package SeisSol (see Data and Resources).

Two alternative fault geometries are considered, a single-fault-plane model (model 1F) and a two-fault-plane model (model 2F). In our simulations, we consider a 1D velocity structure (Woo *et al.*, 2019), off-fault plasticity (Wollherr *et al.*, 2018), depth-dependent bulk cohesion, a rapid velocity weakening friction law, borehole estimates of stress, complex fault geometry, and high-resolution topography.

In the following, we first describe (the Fault Reconstruction section) a new observationally guided fault reconstruction approach based on spatiotemporal clusters of microearthquakes and their spatial uncertainty. In the Fault Strength and Loading Stress section, we analyze initial fault strength and loading stresses using static and dynamic rupture modeling. We then compare the dynamics and kinematics of the two preferred models, models 1F and 2F. The validation of model 2F with regional waveforms as well as a comparison of surface deformation between model 1F and model 2F are also presented in the Results section. Finally, we discuss the importance of considering local stresses loading, apparently weak and critically stressed faults, overpressurized fluids, and dynamic multiple fault interaction in EGS.

MODELING SETUP

In the following, we describe our approach to produce a physically viable model constrained by observational data. Dynamic rupture propagation is governed by fault strength, fault geometry, subsurface material properties, topography, loading ("initial") stresses, nucleation procedure, and empirical friction laws (Dunham *et al.*, 2011a; Harris *et al.*, 2011, 2018). Numerical experiments that vary the aforementioned parameters provide insights into fundamental earthquake physics and allow identifying self-consistent scenarios that explain the mechanical processes of the earthquake as well as observational data.

Fault reconstruction

The detailed fault geometry has a strong effect on the dynamic rupture process (Ando and Kaneko, 2018; Kyriakopoulos *et al.*, 2019; Ulrich, Gabriel, Ampuero, and Xu, 2019; Wollherr *et al.*, 2019). Changes in strike, dip, and deviations from fault planarity can impact the rupture propagation and the corresponding physical processes. The Pohang earthquake occurred on one or several blind and unmapped fault(s). Because the unwrapped Interferometric Synthetic Aperture Radar (InSAR) surface-displacement data show unclear fringes due to small deformation around the epicenter (Choi *et al.*, 2019; Song and Lee, 2019), we use the high-resolution earthquake catalog from Kim *et al.* (2018) to constrain the fault geometry based on a space-time (including their uncertainties in space) clustering approach. The earthquake catalog spans from 9 hr before to 3 hr after the mainshock and contains 217 events.

Spatiotemporal clustering. Clustering techniques allow deciphering complex fault structures by associating seismic

Dynamic rupture modeling aims to reproduce the physical processes that govern how earthquakes start, propagate, and stop for given stress and frictional conditions acting on fault surfaces. The earthquake dynamics are then a result of the model's initial conditions, such as geometry and frictional strength of the fault(s), the tectonic stress state, the regional lithological structure, and a frictional constitutive equation.

[input] stress and frictional conditions acting on fault surfaces (fault plane?)

[output] earthquake

with certain initial conditions:

1. geometry of the fault
2. frictional strength of the fault
3. the tectonic stress state
4. the regional lithological structure
5. frictional constitutive equation

we can reproduce/determine[?] an earthquake with certain features [?]

How can we measure the local and regional stress conditions?

They hypothesized that this earthquake involved failure on two different faults with slightly different focal mechanisms. (Grigoli 2018)

we investigate the dynamic rupture process under variable stress and fault-geometry assumptions for the Pohang earthquake, using the high-performance-comput-ing enabled software package SeisSol

Fault geometry: 1.

2.

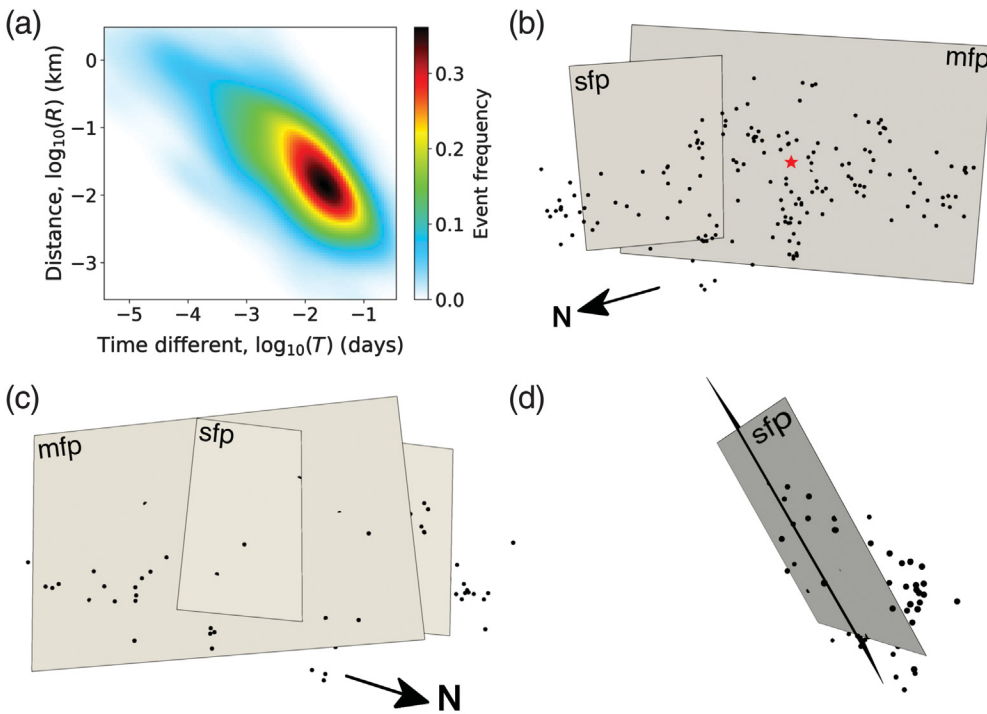


Figure 2. Fault reconstruction using guided anisotropic location uncertainty distribution (g-ACLU). (a) Spatiotemporal density plot of the mainshock and aftershocks based on the nearest-neighbor distance. (b–d) Two-fault-plane geometry inferred by the g-ACLU method. The main fault plane (mfp) has a strike of 214° and dips at 65° , while the secondary fault plane (sfp) has a strike 199° and dips at 60° . Black dots depict the seismicity used in this study. The black arrow points to the north. The geometry of the faults is shown in (b) view from west-northwest along the averaged normal vectors of the two fault planes, in (c) view from east-southeast along the averaged back-normal vectors of the two fault planes, and (d) view from north-northeast along the fault strike direction of the mfp. The red star denotes the hypocenter of the Pohang earthquake.

events to groups (clusters), also discriminating events that are associated with the mainshock from uncorrelated earthquakes (background events); including background events may bias the fault reconstruction algorithm (see the Fault-Plane Fitting section). We examine the seismic sequence to separate seismic clusters and background events using nearest-neighbor distances following Zaliapin and Ben-Zion (2013). The dependence of an event i to a parent event j is determined from the nearest-neighbor distance η_{ij} :

$$\eta_{ij} = dt_{ij} \times dr_{ij}^d, \quad d_{ij} > 0; \eta_{ij} = \infty, \quad d_{ij} < 0, \quad (1)$$

in which $dt_{ij} = t_j - t_i$ is the time between event i and j , $dr_{ij} = (r_j - r_i)$ is the interevent distance between events; r_i = coordinate of event i and r_j = coordinate of event j , and d is the fractal dimension of an earthquake hypocenter distribution (Hirata, 1989). We find that the inferred clusters are not very sensitive to parameter d ; hence, we set $d = 1.6$ following previous studies (Zaliapin and Ben-Zion, 2013; Zhang and Shearer, 2016; Cheng and Chen, 2018). Based on this analysis, all earthquakes of the catalog classify as aftershocks and thus can be associated with the mainshock cluster and can be used

for fault-plane fitting (see Fig. 2a). This cluster is characterized by interevent distances less than 1 km.

Fault-plane fitting. We adopt the anisotropic clustering location uncertainty distribution (ACLD) method, a fault-network reconstruction approach (Wang et al., 2013) that accounts for uncertainties in earthquake locations. This method is extended by considering regional tectonic constraints, focal mechanisms, and surface geological manifestation as prior information, leading to the following improvements in the original ACLUD algorithm:

- 1 Initialize N_0 number of faults following the predefined orientation of the S_{Hmax} extracted from the world stress map with random position and size.
- 2 For each cluster, if more than four similar focal mechanisms (strike, dip, and rake) are available, we

use this information to separate events that have distinct focal mechanisms into other clusters.

- 3 If surface geological manifestation (fault traces) exists (not the case for this study), the strike and dip of the generated fault segment(s) should follow the closest interpreted fault trace orientation.

regional tectonic constrains, focal mechanism, surface geology

We refer to this modified ACLUD method as guided-ACLU (g-ACLU).

All explored solutions are subject to a statistical validation process that examines the likelihood of each proposed fault network, given all available focal mechanisms. Statistical validation uses the Bayesian information criterion (BIC). Initially, the method uses a random number of fault planes. A single fault plane may be split into two separate planes, if the BIC-value remains high. On the other hand, two close-enough fault planes with similar orientation (strike and dip) may be merged into a single fault plane. The process is repeated until the BIC-value reaches a predefined minimum or if the process exceeds the maximum specified number of iterations (Wang et al., 2013).

The ACLUD algorithm by Wang et al. (2013) uses event locations and associated uncertainties given by the earthquake

catalog. We incorporate additional information to increase the robustness of the results and to decrease the explored parameter space. As a priori information, we use the orientation of the maximum compressive regional stress given by the world stress map (Heidbach *et al.*, 2018) and available focal mechanisms in the area that are associated with the earthquake catalog. Therefore, we use a maximum horizontal stress orientation of 74° with an uncertainty of 25° and consider the focal mechanism inferred by Grigoli *et al.* (2018). Because location errors are not specified in this earthquake catalog, we assume that normally distributed uncertainty for all events (standard deviation of 100 m). Kim *et al.* (2018) obtained a median error of 42, 31, and 36 m in the east–west, north–south, and vertical directions, respectively, but no uncertainties for individual events.

Figure 2b–d shows the g-ACLU selected solution, characterized by the smallest BIC-value, which features two intersecting planar fault planes. The main plane strikes at 214° and dips at 65°, whereas the secondary fault plane strikes at 199° and dips 60°, respectively. The two fault planes are separated by a narrow angle of 15°. The secondary fault aligns with the subsidiary fault plane identified by Kim *et al.* (2018). The dimensions of the main and secondary fault planes are 4.3 × 2.8 km² and 3.0 × 2.2 km², respectively. As the goal of this study is to compare the rupture process for two different fault configurations, we define a geometry with one fault plane (model 1F) or with two intersected fault planes (model 2F; derived fault reconstruction analysis). The model 1F has a fault plane striking 214° and dipping 43°, as suggested by Ellsworth *et al.* (2019), Korean Government Commission (2019), and Woo *et al.* (2019).

Material properties

We assume an elastoplastic, isotropic (ISO) medium based on the 1D velocity profile (Fig. S1a, available in the supplemental material to this article; Woo *et al.*, 2019). The velocity profile honors geological structures observed from drilling cores and seismological observations from both active and passive sources, for instance, vertical seismic profiling and well logging (Korean Government Commission, 2019; Woo *et al.*, 2019). The density distribution (Fig. S1a) is adopted from the report by Korean Government Commission (2019).

We use a computationally efficient implementation of a Drucker–Prager off-fault viscoplastic rheology (Wollherr *et al.*, 2018). The off-fault failure criterion is based on the internal friction coefficient (bulk friction) and bulk cohesion. We assume a constant internal friction coefficient equal to the prescribed on-fault friction coefficient ($\mu_{\text{Bulk-Friction}} = 0.6$) for the entire model domain. However, bulk cohesion is set to be depth dependent, accounting for geologic strata in the Pohang EGS site and the hardening of rocks with depth. Therefore, bulk cohesion ranges from $c = 4$ MPa near the surface to $c = 50$ MPa at a depth of 6 km. A lower bulk cohesion (12.5% of the surroundings) is applied in a $1.5 \times 0.3 \times 4$ km³ volume

around the fault intersection for the case of model 2F to mimic pre-existing damage that enhances off-fault yielding and to prevent unrealistic high on-fault stresses at the fault intersection. Off-fault stresses are initialized consistently with the stresses acting on the fault, that is, the on-fault stress state is the resolution of the initial bulk stress tensor onto the surface of every fault element with respect to its individual orientation (with the exception of fault overstressing applied during rupture initiation, see the Nucleation Procedure section). Finally, we set a constant, mesh-independent relaxation time following Wollherr *et al.* (2018) and chose $T_V = 0.05$ s, consistently with choices made in previous studies (e.g., Ulrich, Gabriel, Ampuero, and Xu, 2019; Ulrich, Vater, *et al.*, 2019).

Fault strength and loading stresses

To constrain the azimuth of the principal stress component and the overall stress regime, we extract information (e.g., S_{Hmax} orientation and fault strength) from laboratory and field observations. We then perform numerical experiments to identify the mechanically most viable fault stress and strength configuration supported by observations, that is, the optimal configuration that resolves sufficient shear traction to sustain dynamic rupture on both faults and that promotes fault slip oriented consistently with observations. We adopt a friction law with rapid velocity weakening (adapted from Dunham *et al.*, 2011a; see the Friction Parameters section) that reproduces the rapid friction decrease observed in laboratory experiments at coseismic slip rates (Di Toro *et al.*, 2011).

We parameterize fault friction aiming for realistic levels of static and dynamic frictional resistance and stress drop. All frictional properties are detailed in the Friction Parameters section. We apply velocity weakening ($b - a = 0.004$) across the fault and velocity strengthening ($b - a = -0.004$) to the uppermost part of the fault (see Fig. S1b), which allows for a smoother termination of the rupture there. The state evolution distance (L), initial slip rate (V_{ini}), reference slip velocity (V_0), steady-state friction coefficient (f_0), and weakened friction coefficient (f_w) are constant and depth independent.

We follow the systematic approach of Ulrich, Gabriel, Ampuero, and Xu (2019) to examine initial fault stress and relative apparent fault strength by combining data from observations (e.g., seismotectonic observations and fault fluid pressurization) and the Mohr–Coulomb theory of failure. This workflow reduces the nonuniqueness in dynamic rupture modeling parameter selection by assessing that the stress state is compatible with the fault geometry and the fault-slip orientation (rake angle) inferred from finite source or moment tensor inversion. Assuming a spatially uniform Andersonian stress regime (one principal stress axis is vertical), only four parameters are sufficient to fully describe the stress state and strength of the fault system: the azimuth of maximum compressive stress (S_{Hmax}), the initial relative fault prestress ratio (R_0), the stress shape ratio (v), and the fluid pressure ratio (γ), all detailed hereafter.

The Pohang EGS site is considered to be located within a strike-slip stress regime (Soh *et al.*, 2018, and references therein). This translates into the maximum principal stress being horizontal ($\sigma_1 = S_{\text{Hmax}}$, with principal stress components $\sigma_1 > \sigma_2 > \sigma_3 > 0$) under Andersonian stress. Previous studies examined the azimuth of maximum horizontal stress using different methods, such as borehole and seismological techniques, for example, stress inversion of focal mechanisms (Kim *et al.*, 2017; J. Lee *et al.*, 2017; Soh *et al.*, 2018; Ellsworth *et al.*, 2019; Korean Government Commission, 2019). Soh *et al.* (2018) inferred S_{Hmax} from focal mechanisms of earthquakes that occurred between 1997 and 2016 and determined a regional $S_{\text{Hmax}} = 74^\circ$. However, the earthquakes closest (~40 km) to the Pohang EGS site used in their analysis are the 2016 Gyeongju event and its aftershocks. Based on bore-hole data, Kim *et al.* (2017) and H. Lee *et al.* (2017) determined that S_{Hmax} is about 130° at shallow depths (700–1000 m) within a 10 km radius from the Pohang EGS. In contrast, Ellsworth *et al.* (2019) and Korean Government Commission (2019) inferred a critically stressed thrust-faulting regime. This stress state implies that the vertical stress is the least principal stress under Andersonian stress ($s_v = \sigma_3$). They inferred an S_{Hmax} orientation of $77^\circ \pm 23^\circ$ based on dipole sonic logging data. This orientation is similar to the value of 74° given in the world stress map (Heidbach *et al.*, 2018).

Using numerical simulations, we then assess how these loading-stress regimes for the inferred fault geometry determine nucleation and rupture of the Pohang earthquake. The stress shape ratio v enables a contrast of different stress styles by balancing the principal stress amplitudes. It is defined as

$$v = \frac{(\sigma_2 - \sigma_3)}{(\sigma_1 - \sigma_3)}. \quad (2)$$

For strike-slip regimes ($\sigma_2 = \text{vertical}$), $v < 0.5$ characterizes transpression, $v \approx 0.5$ corresponds to pure strike-slip regime, and $v > 0.5$ characterizes transtension (Ulrich, Gabriel, Ampuero, and Xu, 2019). Soh *et al.* (2018) ($v = 0.12$), Ellsworth *et al.* (2019), and Korean Government Commission (2019) ($v = 0.1$) suggests a stress regime accounting for transpression around the Pohang EGS site (they use different definition of v).

The initial relative prestress ratio (R_0) describes the closeness to failure on a virtual, optimally oriented fault. $R_0 = 1$ indicates a critical stress level on all optimally oriented faults. We can characterize fault strength spatially by calculating the relative prestress ratio (R) on every point of the fault. R denotes the ratio of potential stress drop $\Delta\tau$ with respect to breakdown strength drop $\Delta\tau_b$ for given frictional cohesion (c), static (μ_s), and dynamic (μ_d) friction coefficient (e.g., Aochi and Madariaga, 2003) expressed as

$$R = \frac{\Delta\tau}{\Delta\tau_b} = \frac{\tau_0 - \mu_d\sigma_n}{c + (\mu_s - \mu_d)\times\sigma_n}, \quad (3)$$

in which τ_0 and σ_n are initial shear and normal traction on the fault plane, respectively. However, in this study, we neglect the contribution of frictional cohesion ($c = 0$), which is mostly important to incorporate close to the Earth's surface. We assume $\mu_s = f_0 = 0.6$ and $\mu_d = f_w = 0.1$. The relative prestress ratio R is related to the relative fault strength parameter (S) defined as $S = \frac{1}{R} - 1$. On-fault values of R change at every point as we vary R_0 , taking on values $R \leq R_0$ depending on the orientation of each fault point with respect to the optimal orientation.

The vertical principal stress is assumed to vary linearly with depth, consistent with the geological strata (depth-dependent density [$\rho(z)$] in Fig. S1a). We assume the intermediate principal stress component, σ_2 , to be vertical. The confining pressure of the overlying rock is reduced by the pore pressure (P_f). We assume P_f proportional to lithostatic stress as $P_f = \gamma\rho g z$, in which g is the gravitational acceleration (9.8 m/s^2), z denotes depth (in meters), and γ is the fluid pressure ratio. A fluid pressure ratio of 0.37 indicates hydrostatic pore pressure, whereas $\gamma > 0.37$ implies an overpressurized stress state.

We perform a range of static and dynamic numerical experiments described later to test the sensitivity of the resulting dynamic rupture models to the chosen stress parameterization in terms of S_{Hmax} , R_0 , and γ . We keep the fourth parameter, the stress shape ratio, fixed at $v = 0.12$ (Soh *et al.*, 2018). We do not adjust the stress states for the stress excess during nucleation (see the Nucleation Procedure section). The overstressed nucleation and its parameters are constant for all 180 numerical experiments.

RESULTS

We use the open-source software SeisSol (details in the Numerical Method section) to solve for spontaneous frictional failure on prescribed fault surfaces, Drucker-Prager off-fault plasticity and seismic wave propagation in complex media. We set the on-fault mesh size using estimates of cohesive zone width (details in the Mesh Generation section). We incorporate high-resolution topography into our modeling. Figure 3 shows the computational mesh overlain by a snapshot of absolute velocity at $t = 5 \text{ s}$.

Next, we present 3D dynamic rupture simulations for scenarios that consider one fault plane (model 1F) or two intersecting fault planes (model 2F), incorporating depth-dependent regional loading stresses, off-fault plastic yielding, and high-resolution surface topography. In the preferred model (model 2F), the secondary fault plane is dynamically triggered and can explain the observed non-DC component of the moment tensor solution. Our model is compatible with regional waveforms (see the Model 2F Validation by Regional Waveform Modeling section) and agrees qualitatively with InSAR surface deformation analysis (see the Model 1F and Model 2F Surface Deformations section).

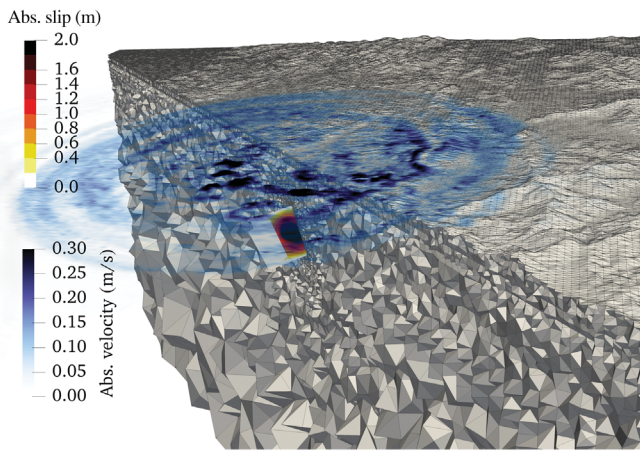


Figure 3. 3D rendering of the unstructured tetrahedral computational mesh, and the fault plane with final slip on the two-fault preferred model (model 2F) of the Pohang earthquake (warm colors, in meters), and the radiated seismic wavefield 5 s after rupture initiation (cold colors, absolute particle velocity in m/s). Note the strong effect of the high-resolution topography on modulating the seismic wavefield.

this is high-resolution topography from GPS measurements of elevation on surface? what is high resolution?

Static and dynamic analysis of initial fault strength and stresses

We first constrain the regional stress from a purely static analysis. Figure S2 shows a few cases we analyzed in detail (see also Table S1). The six examples shown use parameters $\gamma = 0.5$ and $R_0 = 0.7$, and variable $S_{H\max}$ in the 52° – 140° range. According to the static analysis, assuming parameter selection in this study, $S_{H\max} < 87^\circ$ is insufficient to generate a rake angle of shear traction compatible with the thrust-faulting component inferred by the focal mechanism and moment tensor solution. At $S_{H\max} \geq 87^\circ$, a thrust-faulting component starts to emerge. Interestingly, only the secondary fault-plane features a rake angle larger than 40° for $S_{H\max} = 77^\circ$ – 140° . A rake angle of $\sim 80^\circ$, obtained with $S_{H\max} = 120^\circ$, can potentially produce the thrust-faulting component inferred by moment tensor solution. For this parameter selection, the secondary fault plane reaches a higher rake angle of approximately 110° .

We restrict the parameter space for R_0 and γ based on our static analysis. We then explore 180 different dynamic rupture simulations by systematically combining five different values of R_0 , with six different values for γ and $S_{H\max}$, respectively. We vary R_0 in the 0.7–0.9 range, γ within 0.37–0.9 and $S_{H\max}$ within 67° – 120° . Figure 4 summarizes the outcome of 180 numerical dynamic rupture experiments. We find that when assuming $R_0 > 0.8$ and under hydrostatic pore pressure ($\gamma = 0.37$), $S_{H\max} = 120^\circ$ is the only value that promotes self-sustained ruptures in distinction to any other $S_{H\max}$ orientation.

Our modeling suggests that, at least in the framework of the simple parameterization adopted in this study, the thrust-faulting component generated when using $S_{H\max} = 67^\circ$ – 87° is insufficient to explain seismological observations. Such $S_{H\max}$ leads to pure strike-slip faulting as the only mechanical viable

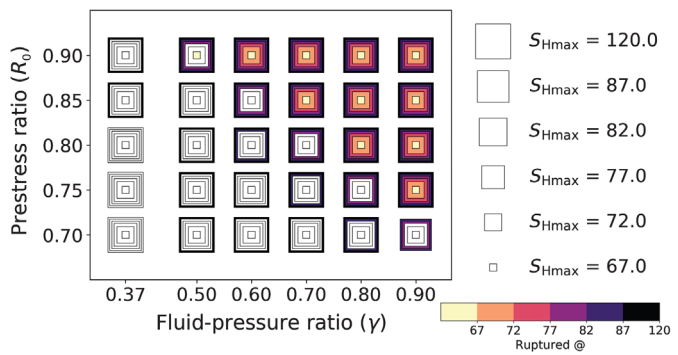


Figure 4. Graphical summary of the outcome of 180 dynamic rupture simulations assuming different combinations of initial relative prestress ratio (R_0), fluid-pressure ratio (γ), and direction of $S_{H\max}$. The corresponding 180 square frames are filled with color, if the combination of parameters is able to trigger self-sustained rupture beyond the nucleation region on any fault. The $S_{H\max}$ direction is indicated by the size of the frame, leading to six imbricated frames for each set of prestress and fluid-pressure ratio parameters.

this is high-resolution topography from GPS measurements of elevation on surface? what is high resolution?

solution. Both dynamic and static analyses suggest that $S_{H\max} = 120^\circ$ is necessary to generate a thrust-faulting component close to the observations. Our analyses allow determining a preferred parameter selection, compatible with inferred ground deformation, observed regional waveforms, and the inferred focal mechanism: $R_0 = 0.8$ and $\gamma = 0.5$.

Rupture dynamics of the preferred scenario model 1F and model 2F

Figure 5a, and Video S1_front and Video S1_back (supplemental material) provide an overview of the simulated earthquake rupture of model 2F: rupture propagates spontaneously across the main fault plane and dynamically triggers the secondary fault plane (rupture jumping).

The rupture nucleates smoothly due to the prescribed time-dependent overstress (see the Nucleation Procedure section) centered at the hypocenter location; it then spontaneously propagates bilaterally across the main fault plane. At a rupture time $t = 0.60$ s, two successive slip-rate fronts emerge, with lower peak slip rates than the main rupture front (two arrows in Fig. 5a, left). This rupture complexity is associated with the simultaneous rupture on both fault planes, leading to multiple reflected and trapped waves in-between the two fault planes, reactivating the main fault around the intersection. Rupture complexity decreases, as rupture on the secondary fault plane terminates. After rupture time $t = 0.80$ s, we observe solely pulse-like rupture propagation across the main fault.

The secondary fault plane is dynamically triggered at $t = 0.4$ s, and its rupture terminates at $t = 0.8$ s simulation time, whereas the main fault stops slipping at $t = 1.5$ s simulation time. The secondary fault-plane ruptures only partially, because its northern segment does not slip (Fig. 5b). High slip

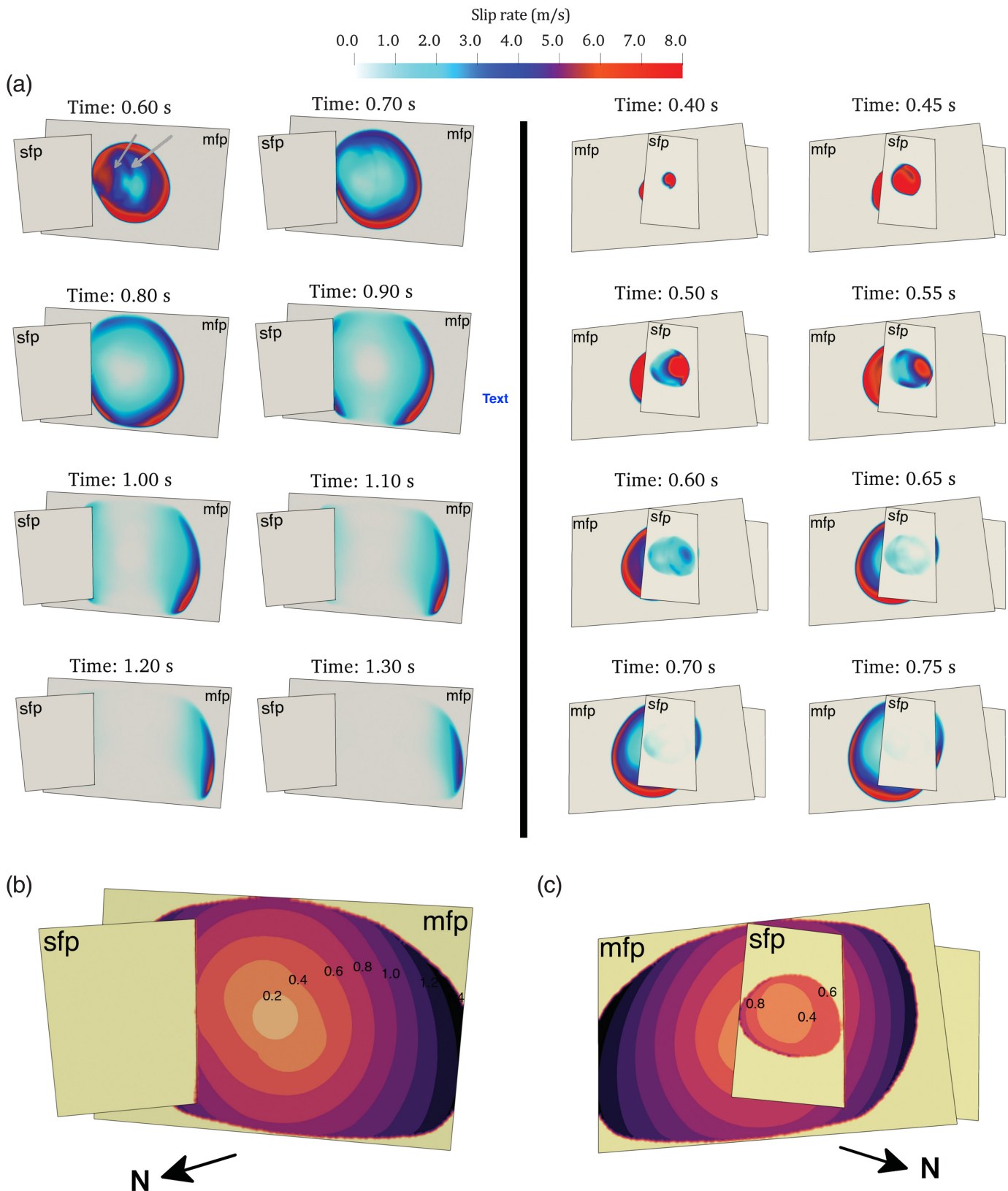


Figure 5. Overview of the simulated earthquake rupture of the preferred model (model 2F), showing in (a) the space–time evolutions of the absolute slip rate (in m/s) across the mfp and sfp. (a, left panel) View from west-northwest along the averaged normal vectors of the two fault planes displaying the main fault rupture. Snapshots every 0.1 s. Two arrows at $t = 0.60$ s indicate the

successive slip rates behind the main rupture front. (Right panel) View from east-southeast along the averaged back-normal vectors of the two fault planes highlighting the rupture of a portion of the secondary fault. Snapshots every 0.05 s. (b,c) Rupture-time contours at intervals of 0.2 s across the mfp and sfp. The black arrow points to the north.

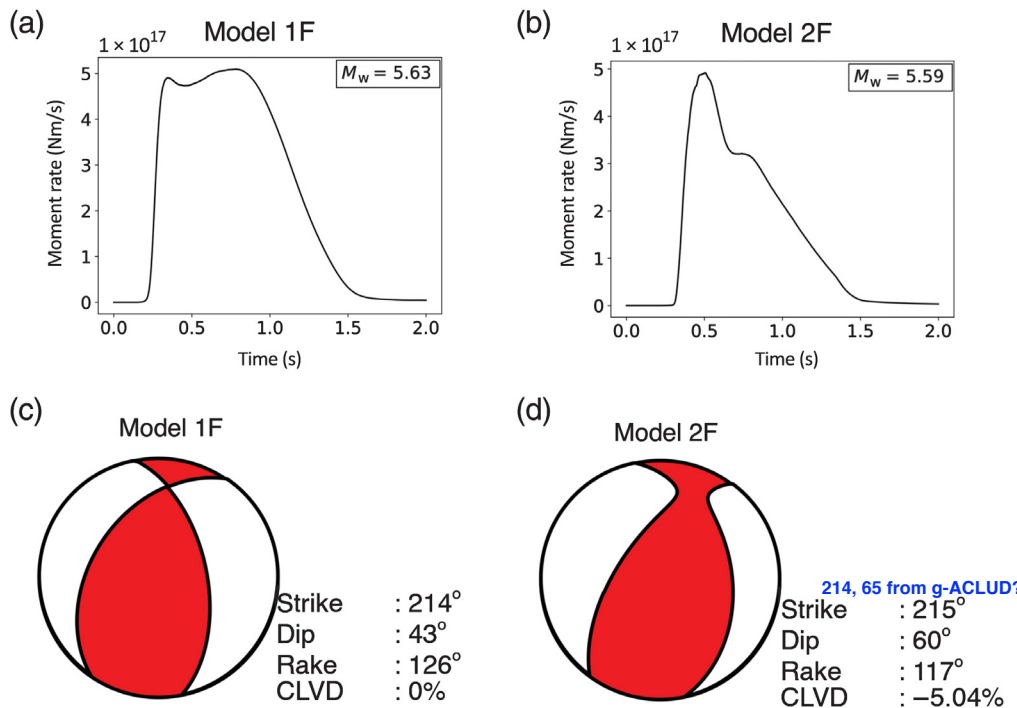


Figure 6. Moment rate release of (a) model 1F and (b) model 2F and moment tensor representation of the preferred (c) one-fault and (d) two-fault models. CLVD, compensated linear vector dipole. ?

rates (~ 10 m/s, warm colors in Fig. 5a, right) and multiple rupture fronts occur near the fault intersection at the secondary fault. Rupture heals close to the fault intersection region around $t = 0.65$ s.

After $t = 0.80$ s, rupture on the main fault dynamically clamps (e.g., Kyriakopoulos *et al.*, 2019) and thus does not facilitate direct branching to the northern unbroken part of the secondary fault plane. We observe asymmetric peak slip-rate distribution (see Fig. S3), with higher values on the left of the main fault plane (Fig. 5a, right panel) and lower peak slip rates in which ruptures across directly adjacent fault planes interact, which is also associated with high off-fault plastic yielding (see the Off-Fault Deformation section). The entire rupture is completed after $t \sim 1.5$ s simulation time, breaking ~ 4 km of fault length and generating a moment magnitude of $M_w 5.59$ (dominated by slip on the main fault plane). We find that rupture stops smoothly and spontaneously on the secondary fault plane and northeastern part of the main fault plane, while being stopped abruptly by the southwestern fault end of the main fault plane.

In contrast to the model 2F, the preferred single-plane fault model, model 1F, produces symmetric bilateral slip-rate and slip distributions.

Rupture kinematics of the preferred model 1F and model 2F scenarios

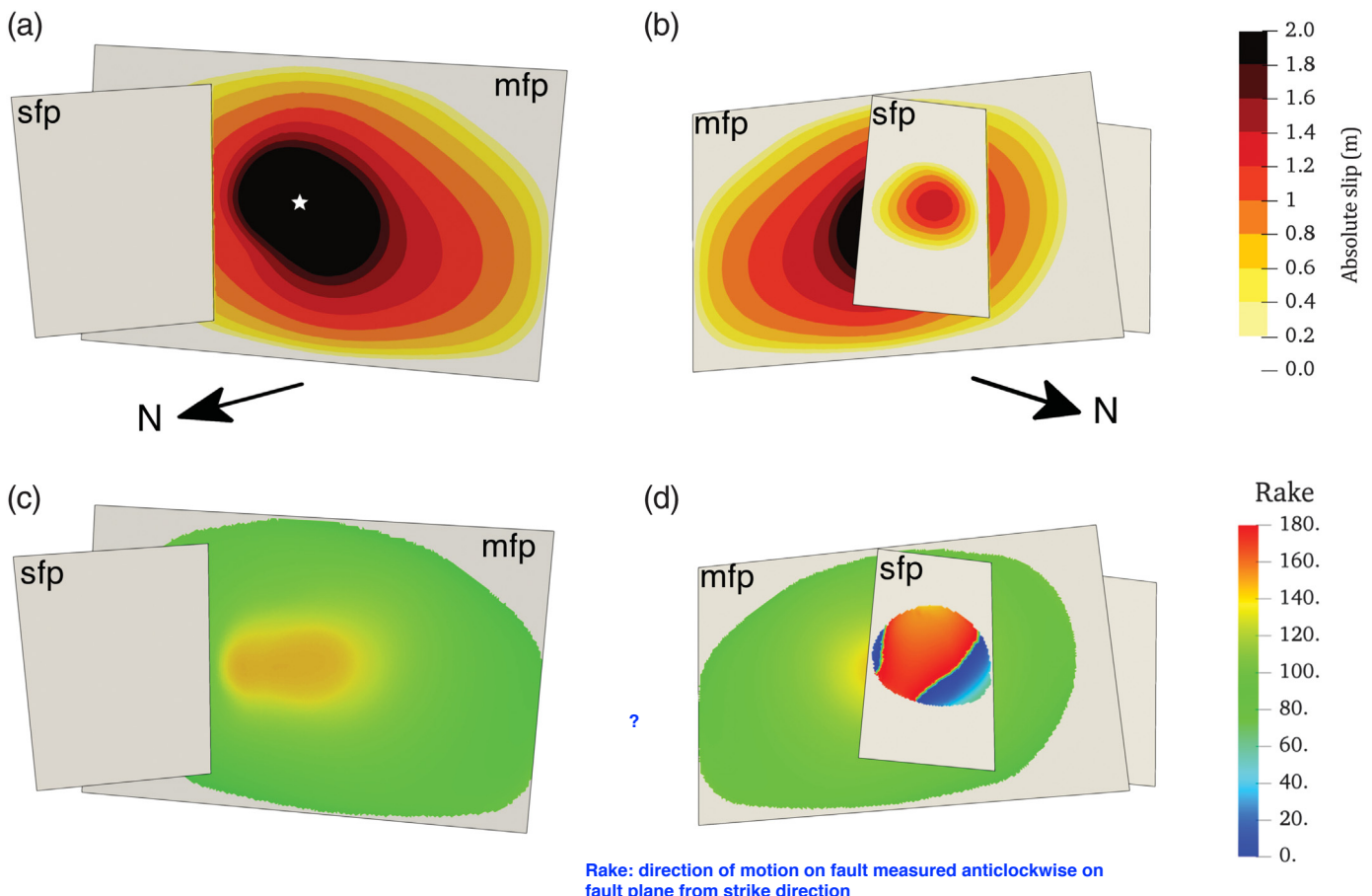
Because of the size of the event and limited available data, the kinematics of the Pohang earthquake are challenging to be

quantified from source inversion. We here describe the model kinematics of the preferred model 1F and model 2F earthquake scenarios and then compare both with two observational studies (Grigoli *et al.*, 2018; Song and Lee, 2019).

Song and Lee (2019) estimated the static slip distribution by InSAR (both descending and ascending-descending orbit) for a single fault plane with patch size 0.5×0.5 km 2 . Higher slip predominantly occurs northeast of the hypocenter, with an average slip of 0.15 m (Song and Lee, 2019). Grigoli *et al.* (2018) applied an empirical Green's function technique to study rupture duration and directivity, suggesting an apparent rupture duration of ~ 1 and ~ 3 s for stations observed in the southeast and northwest directions, respectively. Their focal mechanism shows an average rake of $\sim 130^\circ$.

The two dynamic rupture scenarios differ slightly in moment magnitude, $M_w 5.63$ and $M_w 5.59$ for model 1F and model 2F, reflecting different fault geometries while otherwise using the same model parameter selection. We point out that most slip of model 2F occurs on the main fault—its magnitude is reduced to $M_w 5.51$ when removing the subsidiary plane.

The resulting synthetic source time functions of model 1F and model 2F are presented in Figure 6a and 6b, respectively. The boxcar-shaped moment rate function of model 1F results from its relatively simple rupture dynamics across one planar fault. Model 2F features a more complicated moment rate function with two peaks of which the first one is reached at $t = 0.5$ s simulation time during simultaneous rupture of both fault planes. The rupture duration of each scenario is less than 1.5 s simulation time. The moment tensor representations of model 1F and model 2F are presented in Figure 6c and 6d, respectively. Both scenarios show oblique faulting mechanisms. Model 1F clearly produces a DC moment tensor solution (Fig. 6c), whereas the model 2F yields a non-DC solution due to complex source mechanism (Fig. 6d), consistent with Grigoli *et al.* (2018). Nevertheless, our simulation produces a smaller amount of compensated linear vector dipole (CLVD) compared with Grigoli *et al.* (2018). The equivalent moment tensor solution of model 2F can be decomposed,



following the methodology of Vavryčuk (2015), into 82.95% DC, -5.05% CLVD, and -12% ISO components. In contrast, Grigoli *et al.* (2018) find -37% CLVD. In our simulations, model 2F's rupture is characterized by an average rupture speed (v_r) of $v_r \approx 2250$ m/s, well below the average Rayleigh wavespeed (V_S) at the depth of the faults ($v_r \approx 0.75V_S$). The spatial variation of v_r is mainly related to the complexity of rupture around the intersection for both, the main and secondary fault planes. We observe higher average rupture speed $v_r \approx 2780$ m/s ($v_r \approx 0.8V_S$) on the secondary fault plane (see rupture contours every 0.2 s in Fig. 5b,c). We note the localized occurrence of supershear rupture speed (~ 4000 m/s) near the edge of the prescribed nucleation patch of the main fault reflecting the high overstress required for initiating the preferred rupture dynamics in our setup. Also, the secondary fault-plane features localized supershear episodes (~ 3800 m/s). In our model setup, this may be related to locally high fluid overpressure, and/or reflect the low resolution and 1D restriction of the used velocity model. More complex fluid effects have been shown to facilitate the transition to sub-Rayleigh to supershear ruptures in fully coupled 2D models (Jin and Zoback, 2018).

In our preferred model, high slip (~ 2 m) occurs in the center of the main fault. We observe a maximum slip of 1.3 m at the secondary fault plane (Fig. 7b). In total, the average on-fault slip is 0.32 m. Model 1F and model 2F both feature

Figure 7. Distribution of absolute fault slip (in meters) in (a,b), and rake angles (in degrees) in (c,d) for the preferred dynamic rupture scenario (model 2F) across the mfp and sfp. (a,c) View from west-northwest along the averaged normal vectors of the two fault planes highlighting the main fault rupture. (b, d) View from east-southeast along the averaged back-normal vectors of the two fault planes highlighting the rupture of a portion of the secondary fault. The white star in (a) marks the considered hypocenter location.

higher slip than Song and Lee (2019) infer in their static slip inversion. In addition, differences may arise due to different modeling assumptions in terms of fault dimensions and shear moduli. First, Song and Lee (2019) assume a slightly larger shear modulus of $G = 30$ GPa than in our model ($G = 26$ GPa). Second, they assume a single fault plane of significantly larger dimensions ($6 \times 5 \text{ km}^2$) than the faults of our models (see the Fault Reconstruction section). This large fault geometry allows for the possibility of near-surface slip.

The orientation of fault slip is modulated by the dynamic source process. The dynamic interaction of the two fault planes induces a moderate thrust-faulting component (rake $\sim 135^\circ - 150^\circ$) on the main fault plane, as well as complex time-dependent rake orientations on the secondary fault (see also Fig. 7c,d). In contrast to model 2F, the orientations of the final rake angle of model 1F are distributed more homogeneously, with an average of 127° . The rake of model 1F is different from model 2F due to different dip angles of the main

fault (43° in model 1F). This average rake angle is comparable to the focal mechanism derived by Grigoli *et al.* (2018) (rake of 130°). The average on-fault slip is 0.35 m. We observe that, on average, the rupture speed is $v_r \approx 2400$ m/s. Reflecting similar dynamic parameters to model 2F, model 1F also experiences supershear rupture near the nucleation patch.

Waveform comparison for model 1F and model 2F

Is far-field seismic recordings more reliable?

In the following, we analyze the differences between model 1F and model 2F in terms of near and far-field ground motion. Hereinafter, all distances from the fault are considered as Joyner–Boore distances (R_{JB} , the shortest distance from a site to the surface projection of fault planes). We compare synthetic waveforms computed for hypothetical (“virtual”) stations located close (~ 4 km) and far (> 20 km) from the epicenter.

Figure 8b shows three-component waveforms at 19 randomly located virtual stations (Fig. 8a). We place 10 stations near the epicenter (~ 4 km horizontal distance) to inspect near-field seismic-waveform characteristics. We filter all synthetic waveforms in the frequency band of 0.1–2 Hz using a fourth-order Butterworth filter. Figure 8c depicts all three-component velocity waveforms. Overall, waveforms of model 1F and model 2F are very similar in this frequency range, but waveforms from model 1F have systematically higher amplitudes from magnitude? 1F is slightly higher in magnitude than model 2F. The most remarkable amplitude differences occur on the east–west component for stations 004, 008, 009, and 010, which are all located above or close to the faults.

At some stations, distinct waveform differences appear (e.g., the north–south component of stations 007, 014, 011, and 019); these stations are mostly located on the hanging wall. After 5 s, once the rupture is fully arrested, differences vanish, and waveforms become comparable for both models. As depicted in Figure 8b, stations located close to the region where faults overlap in model 2F show significant differences in seismic-wave signatures on the horizontal components. We conjecture that the additional secondary fault defocuses ground motions and thus generates different waveforms.

Why distinct waveform differences appear mostly on stations located on the hanging wall?

Off-fault deformation

Our preferred dynamic earthquake rupture model 2F reveals significant off-fault plastic deformation in the vicinity of geometric fault complexity, similar to recent simulations for the 1992 Landers earthquake (Wollherr *et al.*, 2018), the 2016 Kaikōura earthquake (Klinger *et al.*, 2018), and the 2019 Ridgecrest earthquake sequence (Taufiqurrahman *et al.*, 2019). Here, significant off-fault plastic deformation (quantified as the scalar quantity η following Ma, 2008; Wollherr *et al.*, 2019) occurs (1) in the pre-existing damage zone at the fault intersection, (2) at the dilatational side of the main and the secondary faults (as expected from previous theoretical and numerical studies, given the shallow angle of both faults and $S_{H\max}$; Templeton and Rice, 2008; Gabriel *et al.*, 2013), and (3) close to the free surface (see Fig. S4c,d).

The fault intersection of model 2F elevates the total off-fault plasticity response, diminishing high on-fault stresses while limiting peak slip rates and reducing peak ground motions (Andrews, 2005; Dunham *et al.*, 2011a; Gabriel *et al.*, 2013; Roten *et al.*, 2014; Wollherr *et al.*, 2018). When comparing waveforms, we also notice overall lower velocity amplitudes (compared with model 1F) on the near-fault stations caused by the combined effects of fault complexity and off-fault yielding. Interestingly, the stronger plastic yielding response in model 2F leads to lower variability (not shown here) in ground motions (peak ground velocity [PGV]; as in Wollherr *et al.*, 2019), even though the fault geometry is more complex.

Model 1F and model 2F surface deformations

Next, we compare the coseismic surface displacement generated by model 1F to model 2F (Fig. 9a,b). We translate the synthetic vertical and horizontal displacements into line-of-sight (LoS) displacement components.

The spatial distribution of coseismic surface deformation is noticeably different. Model 1F features higher LoS displacements in southeastern direction relative to the Gokgang fault (~ 2 km from the bay) compared with model 2F (~ 5 km from the bay) and generates on average lower negative LoS displacements. Model 1F creates a wider area of uplifted LoS displacements, which resembles an ellipse with a major axis of 6 km and a minor axis of 4.1 km. The most prominent spatial differences are (1) the vertical LoS displacements of model 1F are slightly shifted to the east relative to the epicenter and (2) the location of zero displacements in between positive LoS displacements (in the region of the epicenter) and negative LoS displacements at the eastern-to-southward of the epicenter. Model 2F produces an average of 5 cm subsidence, whereas model 1F only produces 2 cm average subsidence. This can be attributed to model 1F’s more shallow-dipping angle. The coseismic surface displacements of model 2F compare better with InSAR ground deformation inferences of Song and Lee (2019) than those of model 1F in terms of the location of the pivot line delimiting positive and negative LoS displacements (~ 4.5 km from the bay).

Although synthetic (model 2F) and observed surface displacements significantly differ locally and quantitatively, they reveal qualitatively comparable large-scale features. The following observations are captured by model 2F: (1) uplift to eastward displacement is observed near the epicenter and (2) the uplifted area forms an ellipse-like shape with a major axis of ~ 5.6 km and a minor axis of ~ 3.8 km. Correspondingly, Pohang city also experienced subsidence according to field observations (Kang, Kim, Bae, *et al.*, 2019; Kang, Kim, Cho, *et al.*, 2019). In addition, our synthetics also suggest subsidence underneath the bay.

Although the contribution of the secondary fault plane is critical to reproduce the inferred non-DC component, comparison of synthetic coseismic surface displacements of model

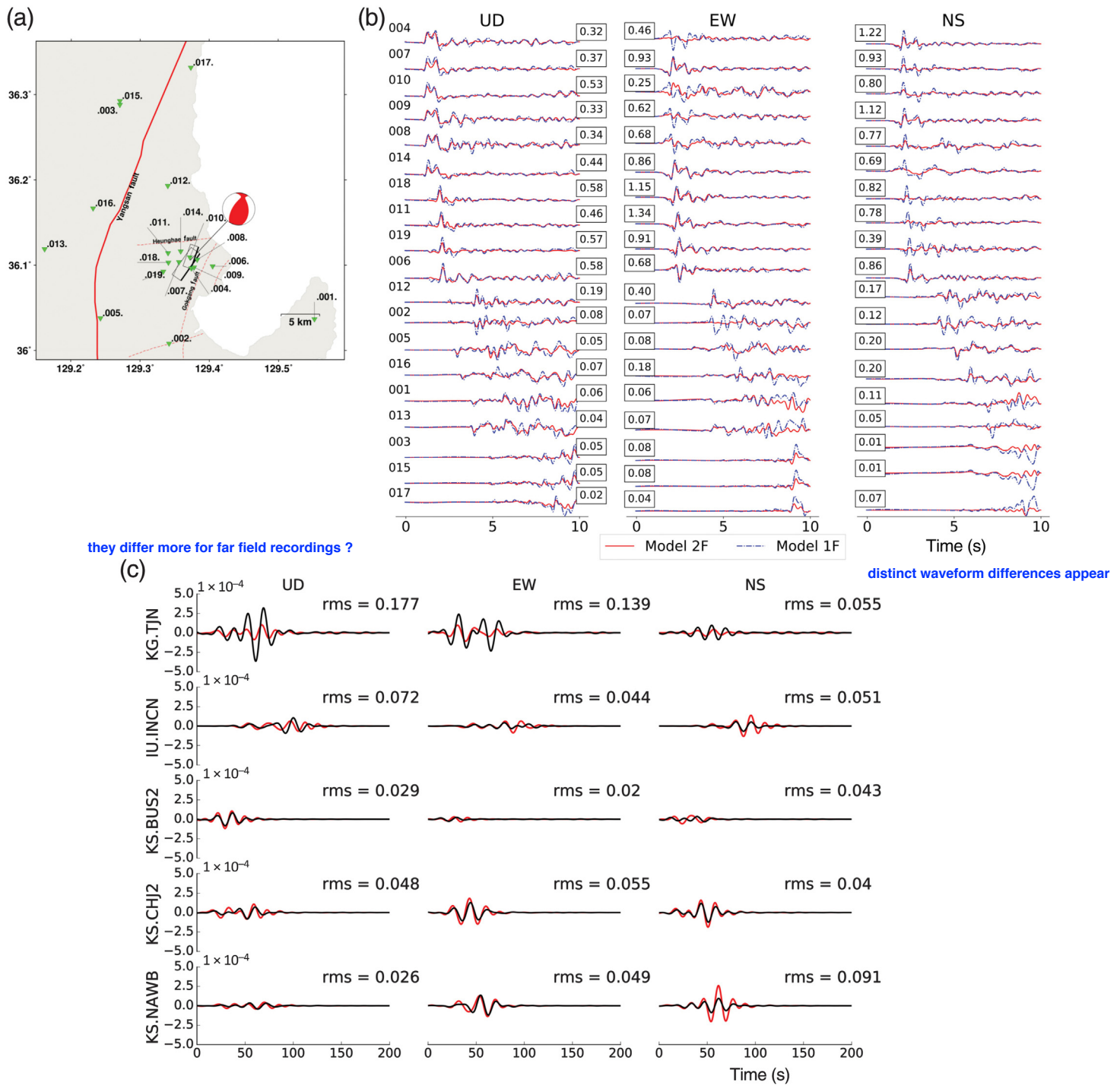


Figure 8. Comparison of synthetic and observed ground motion waveforms. (a) Distribution of virtual stations (green triangles) at which synthetic waveforms are compared in (b). The focal mechanism plot is the moment tensor representation of the preferred two-fault-plane model scenario (model 2F). Solid and dashed red lines represent the mapped Yangsan fault surface trace and the interpreted fault traces near the Pohang EGS site, respectively. Two rectangles show the location and geometry of the faults used in this study. (b) Comparison of synthetic waveforms using one (model 1F, blue dashed lines) and two fault planes (model 2F, red solid lines) at the 19 dummy stations located in (a). A 0.1–2 Hz fourth-order Butterworth filter is applied to all traces. All traces are normalized. For each trace, the

maximum velocity amplitude (in m/s) of model 1F is indicated within a black square. (c) Observed (black) and synthetic (red) waveforms for five regional stations for up-down (UD), east-west (EW), and north-south (NS) components (all located in South Korea, see blue triangles in Fig. 1). $t = 0$ s denotes the origin time of the Pohang earthquake. A 0.033–0.08 Hz fourth-order Butterworth filter is applied to all traces. Synthetic regional waveforms are generated from the preferred dynamic rupture scenario model 2F using Instaseis (Krischer et al., 2017) and 2 s accurate Green's functions based on the preliminary reference Earth model anisotropic model. Rms, root mean square.

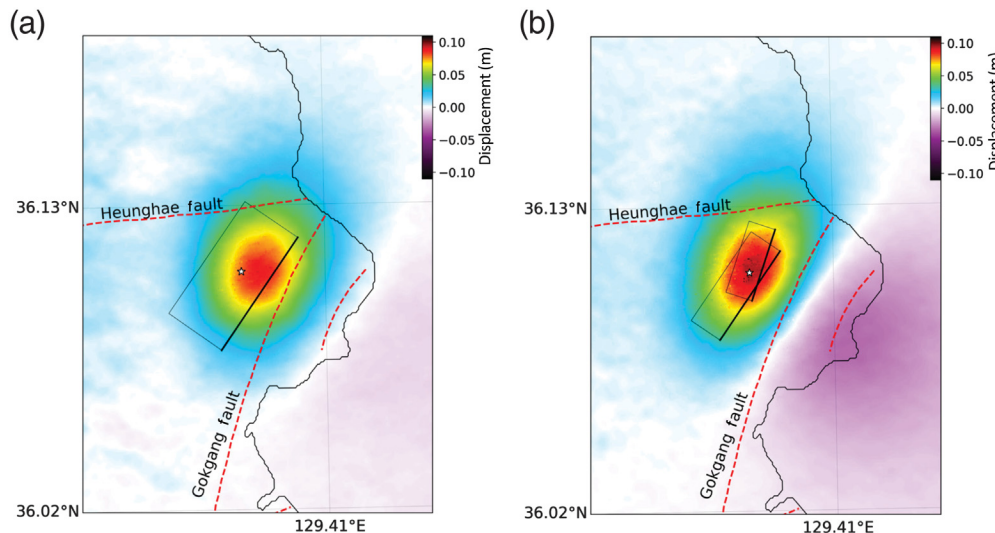


Figure 9. (a,b) Modeled coseismic surface displacements in the Interferometric Synthetic Aperture Radar line-of-sight direction (in meters) generated by (a) model 1F (rectangle) and (b) model 2F (two rectangles), respectively. Dashed red lines represent the traces of the interpreted faults near the EGS site.

2F with and without the secondary fault (see Fig. S5a) suggests that the contribution of the secondary fault plane to the ground displacement is small (Fig. S5b), as expected from its small slip contribution. We note that the InSAR data may not be sensitive enough to discriminate between a one- and a two-fault-plane models.

2 models differ in subsidence

Restoration of clipped seismic waveforms using projection onto convex sets method

Model 2F validation by regional waveform modeling

Unfortunately, a local seismic network of eight portable seismic stations (Kim et al., 2018) deployed around the EGS site produced saturated (clipped) seismograms. Therefore, we choose to compare synthetic waveforms with regional recordings at five stations surrounding the Pohang EGS site (see Fig. 1) at epicentral distances of approximately more than 70 km.

Synthetic seismograms for model 2F compare well with corresponding regional low-frequency seismic-wave observations (Fig. 8c). Synthetic waveforms are calculated using a Green's function database of teleseismic waveforms (Instaseis, Krischer et al., 2017). We transform the dynamic rupture model into a single moment tensor representation following Ulrich, Gabriel, Ampuero, and Xu (2019) and Ulrich, Vater, et al. (2019). The Green's function database we use is based on the anisotropic preliminary reference Earth model (PREM) and is accurate to a minimum period of 2 s. Synthetic and observed waveforms are filtered in the frequency range 0.033–0.08 Hz using a fourth-order Butterworth filter, equivalent to the frequency band used in the source inversion of Grigoli et al. (2018). The goodness of fit is assessed by the root mean square misfit.

Although the synthetic waveforms generally compare reasonably well with regional recordings, we find that synthetic amplitudes are larger than the observed data at few stations (e.g.,

north-south components of stations IU.INCN, KS.BUS2, KS.CHJ2, and KS.NAWB). We attribute this to the usage of a 1D PREM model, which is more suitable for modeling synthetics at larger azimuthal distance. In addition, the fact that our simulation returns a slightly higher seismic moment than observed and is not able to fully capture non-DC components of the source may play a role. In addition, the large misfit at station KG.TJN on the up-down and east-west components may be attributed to unmodeled site effects. We quantitatively compare low-frequency (0.033–0.08 Hz) synthetics generated by a point source representing the dynamic rupture model 2F

to the ones corresponding to the inferred moment tensor solution of Grigoli et al. (2018) (see Fig. S6). Our synthetics do not differ significantly from the synthetics of Grigoli et al. (2018), which are derived by full-waveform inversion of the waveforms recorded at stations KS.BUS2, KS.CHJ2, and KS.NAWB. Notable differences are limited to the horizontal components of station KS.BUS2 and the vertical component of station KS.NAWB.

? compare our synthetic low-frequencies generated by a point source with moment tensor solutions

DISCUSSION

The importance of local stresses for rupture dynamics in EGS

Previous studies examining stress regimes and maximum horizontal stress orientation around the Pohang EGS site provided varying interpretations, thereby motivating our systematic numerical experiments in the Static and Dynamic Analysis of Initial Fault Strength and Stresses section, considering various loading stress settings. Assuming a spatially uniform Andersonian stress regime, we find that an initial stress state constrained by regional stress inversions is unable to generate the observed thrust-faulting component of the Pohang earthquake. This suggests significant local deviations from the regional stress state near the Pohang EGS site. Kim et al. (2017) and H. Lee et al. (2017) infer the stress orientation at short epicentral distance (<10 km) from borehole image log data acquired prior to the Pohang earthquake. However, these data are limited to 1 km depth, whereas the Pohang earthquake hypocentral depth is much deeper, with an estimated depth of 4.27 km. Ellsworth et al. (2019) note that the in situ stress state at the Pohang EGS site is transpressional based on dipole sonic logging of the PX-2 well.

From our static numerical experiments, we infer that a pure strike-slip stress regime ($\sigma_2 = s_v$) and $S_{H\max} = 120^\circ$ yield

a thrust-faulting component consistent with observations (Fig. S2). This finding is corroborated by our dynamic rupture simulations under identical loading (Fig. 6c,d). We also observe that under these conditions spontaneous rupture propagation is favored. In contrast, exploring also a reverse faulting regime ($\sigma_3 = s_v$) accounting for low $v = 0.1$ across the entire fault planes, as suggested by Ellsworth *et al.* (2019), does not yield sufficiently high shear tractions on our fault system, leading to rapid cessation of dynamic rupture.

Local variations of the stress state around EGS sites, including the Pohang EGS site, have been observed in hydraulic stimulation experiments of crystalline-rock reservoirs (Schoenball *et al.*, 2010), in data-driven geomechanical analysis (Cuenot *et al.*, 2006; Hardebeck and Michael, 2006; Martínez-Garzón *et al.*, 2013, 2014; Schoenball *et al.*, 2014) and in numerical experiments (Jeanne *et al.*, 2015; Ziegler *et al.*, 2017). Such spatial and temporal stress reorientation is typically a direct response to hydraulic stimulation and fluid injections (Cornet *et al.*, 2007; Schoenball *et al.*, 2010, 2014; Ziegler *et al.*, 2017; Liu and Zahradník, 2020).

In the geothermal field surrounding the Geysers in California, Martínez-Garzón *et al.* (2014) found that the stress regime changed from normal faulting to strike slip near the injection wells. At the Pohang EGS site, local variations in the stress regime have been inferred from focal mechanisms of microearthquakes before and after the Pohang earthquake. Woo *et al.* (2019) reported strike-slip faulting north of the hypocenter to strike-slip associated thrust-faulting and pure thrust-faulting components toward the south before the mainshock. After the mainshock occurred, aftershock focal mechanisms were mainly strike slip in the southwest to oblique faulting in the northeast (Kim *et al.*, 2020). Changes in stress orientations and stress regime near the hypocenter prior to the mainshock are due to hydraulic stimulation and fluid injections (Martínez-Garzón *et al.*, 2014; Liu and Zahradník, 2020). Those changes may be related to elevated pore pressure and the corresponding changes in poroelastic stresses (Cuenot *et al.*, 2006; Martínez-Garzón *et al.*, 2014; Schoenball *et al.*, 2014; Jeanne *et al.*, 2015). Lim *et al.* (2020) evaluate the spatiotemporal changes in poroelastic stresses associated with fluid injection in the Pohang region and suggest that slow fluid diffusion could have resulted in Coulomb stress changes of up to 1.1 bar.

Based on the analysis of our numerical experiments, we deduce that our models are highly sensitive to variations in the initial stress state and, therefore, allow for finely constraining the fault stress loading parameters. For example, a small change in S_{Hmax} may induce a significant change in the modeled focal mechanism. All faults are exposed to the same local stress regime while experiencing varying ratios of shear and normal loading, depending on their orientation toward this loading. Even a small change in fault geometry (e.g., in strike, dip, size, and the angle between fault planes) strongly affects the dynamic rupture result (e.g., Yamashita and

Umeda, 1994; Aochi *et al.*, 2005; Bhat *et al.*, 2007; Ulrich, Gabriel, Ampuero, and Xu, 2019; van Zelst *et al.*, 2019), as illustrated when comparing model 1F and model 2F. We point out that trade-offs between the inferred stress state and fault geometry can be readily explored, if new observations become available.

As model 2F comprises two intersecting fault planes with only small differences in strike and dip (15° in strike, 5° in dip), both planes may be considered part of a single (wide) fault zone (e.g., Chester *et al.*, 1993; Caine *et al.*, 1996; Mitchell and Faulkner, 2009). A large fraction of friable round-shape mud balls suggests a fault-zone width of less than 200 m (Ellsworth *et al.*, 2019), to be compared with a maximum distance of ~750 m between the two faults of model 2F.

Complex volumetric failure patterns have been inferred for recent well-recorded small and large earthquakes (e.g., Cheng *et al.*, 2018; Ross *et al.*, 2019; Taufiqurrahman *et al.*, 2019) and may be promoted by local stress perturbation. In our model 2F, off-fault plastic deformation accumulates close to the fault intersection (Fig. S4), indicating that the local fault-zone structure may be more complex than our model 2F.

In summary, these observations support our assumption on the loading stress, which is consistent with Ellsworth *et al.* (2019) in the nucleation region, but differently oriented everywhere else. Complexities in the in situ stress state are expected in the region where the Pohang earthquake occurred, due to the history of hydraulic stimulations. That is, the EGS operation itself perturbs the local stress conditions in a manner that makes it more difficult to assess the potential seismic hazard at the EGS site, while usually hazard assessment is conducted in advance utilizing the unperturbed regional stress information.

The importance of critically stressed, static and dynamic weak faults, and overpressurized fluids

Our experiments (Fig. 4) emphasize the necessity of assuming overpressurized fluids ($\gamma > 0.37$) and a close to critical stress state. All models adopt rapid frictional weakening characterized by a large friction drop (Table A1). Fluid pressure, initial relative fault strength (parametrized by R_0), and friction drop jointly control the expected (dynamic) stress drop in each simulation. An a priori order-of-magnitude estimate of stress drop can be written as: $R_0(1 - \gamma)\sigma_c(\mu_s - \mu_d)$ (equation 18 in Ulrich, Gabriel, Ampuero, and Xu, 2019), which highlights the interdependency of a realistic stress drop, strong dynamic weakening, fluid pressure, and resolving sufficient shear tractions with the expected slip direction.

A critically stressed state has been suggested by Ellsworth *et al.* (2019) by analyzing dipole sonic logging data at the Pohang drilling site. In our preferred model 2F, we use the ratio of shear stress over effective normal stress ($\frac{\tau}{\sigma_n}$) to quantify fault strength, and find ratios of 0.54 and 0.59 for the main and secondary fault planes, respectively. This fault strength is close to the assumed steady-state friction coefficient ($f_0 = 0.6$),

indicating that the faults are close to failure just prior to rupture nucleation and thus close to critically stressed.

In our preferred model, both faults are nonoptimally oriented with respect to the local stress conditions. The relative prestress ratio is $R = 0.35$ on the main fault and $R = 0.4$ on the secondary fault plane, which is less than our assumed $R_0 = 0.8$. According to Andersonian faulting theory, fault strength is related to its orientation with respect to the regional stress. Here, the main fault plane is oriented at 54° and the secondary fault at 60° relative to the regional maximum compressive stress ($S_{H\max} = 77^\circ$). Thus, the two-fault system would be considered weak in the classic static sense.

All modeled faults in this study weaken dramatically at coseismic slip rates while stress drops are limited by the elevated fluid pressure. Besides resembling the dramatic friction decrease observed in laboratory experiments and the theory of thermal weakening processes, previous dynamic rupture studies utilizing rapid velocity weakening using low values of fully weakened friction coefficient (f_w) reproduced rupture complexities, such as rupture reactivation and pulse-like ruptures, without assuming small-scale heterogeneities (e.g., Gabriel *et al.*, 2012).

In our simulation, we use a fluid pressure ratio of $\gamma = 0.5$, which corresponds to a reduction of the normal stress of approximately 14.3 MPa compared with a hydrostatic state. The reduction in effective normal stress mechanically lowers the static strength of faults. Our assumption of high fluid pressure may relate to various episodes of drilling mud loss (reported to have occurred on 30–31 October 2015 at 3800 m depth), suggesting an increase of fluid pressure on the order of 20 MPa around the borehole, and the fluid injection operations (Ellsworth *et al.*, 2019; Korean Government Commission, 2019).

The importance of fault interaction for the dynamic rupture process and faulting mechanism

In our preferred model (model 2F), the secondary fault only partially ruptured during the Pohang earthquake. Strong variations in slip rate associated with dynamic rupture complexity across two fault planes and their interaction, spontaneous rupture arrest, and the asymmetrical accumulated fault slip on the main and secondary fault planes could potentially favor dynamic and static Coulomb stress transfers that facilitate a later activation of the unruptured area of the secondary fault. The largest aftershock (less than 3 hr after the mainshock at 650 m epicentral distance, northwest of the mainshock) may have occurred in such an unruptured area on the secondary fault.

In our model, complex shear faulting across two fault planes induces a non-DC component, which, however, is considerably smaller (14%) compared to the CLVD component inferred by Grigoli *et al.* (2018). Additional factors not considered in this study may contribute to an apparent non-DC component, such as strong deviations from fault planarity (larger scale curvature and small-scale roughness, e.g., Shi and Day, 2013; Bydlon and Dunham, 2015; Mai *et al.*, 2018; Ulrich, Gabriel, and Uphoff,

2019), stronger heterogeneities in fault stress and strength (Ripperger *et al.*, 2008), and 3D subsurface structure (e.g., Pelties *et al.*, 2015). However, rupture complexity is also increased when incorporating tensile faulting, poroelastic rheology, and source or propagation anisotropy (Julian *et al.*, 1998; Boitz *et al.*, 2018). The CLVD contribution may also increase when assuming a larger number of faults. Although the limited data available do not suggest rupture of additional fault planes, stochastically distributed and dynamically activated fracture networks (e.g., Anger and Gabriel, 2019; Okubo *et al.*, 2019) around the main fault are expected given the ongoing stimulation operation.

Importance of dense seismic monitoring during EGS projects

The complex interaction of local stress loading and fault strength conditions, rupture dynamics, and fault interaction on multiple fault segments presented here highlights the importance of and need for a dense local seismic network within the operational areas for monitoring and analyzing microseismicity before, during, and after EGS operation. Pre-EGS stimulation seismic monitoring is needed to define the “unperturbed state” of the system (the rock volume to be stimulated) and for characterizing potentially unmapped fault(s) that may interact during cascading rupture; such seismic monitoring may be accompanied by detailed borehole logging to assess the local stress state prior to stimulation.

During the stimulation and operational phase, a dense seismic monitoring network is critically important to facilitate high-precision and high-fidelity seismic source studies (Kwiatek *et al.*, 2019; Hillers *et al.*, 2020). In conjunction with detailed operational fluid-injection parameters, the reservoir stress state and its susceptibility for generating earthquakes can be assessed (Galis *et al.*, 2017; Kwiatek *et al.*, 2019). The available recordings of the operational monitoring seismic network near the Pohang EGS site were saturated (clipped) by the unexpected high-magnitude earthquake; therefore, we propose to install accelerometers as complementary instrumentation in EGS monitoring networks. In addition, the rise of distributed acoustic sensing opens new opportunities as an additional seismic monitoring network, especially for EGS that is located in urban areas (Zhan, 2019).

Our study suggests that fully physics-based numerical simulations prior, during, and after an EGS project may be useful to not only gain a first-order understanding of potential effects and consequences of the EGS experiments (e.g., risk-prone area as reflected by peak ground motions; PGVs, Fig. S7), but also to optimally design the seismic monitoring network to ensure that all vital data are collected as needed for future monitoring and mitigation purposes.

CONCLUSIONS

A guided fault reconstruction approach that clusters spatio-temporal aftershock locations accounting for their uncertainty

is applied to **create the geometry** for a dynamic rupture model that comprises two fault planes and that reproduces key characteristics of the Pohang earthquake. **Rupture complexity is arising from the dynamic interaction of two failing fault planes with shallow intersection angles.**

Static Mohr-Coulomb failure analysis and **180 numerical simulations** demonstrate that the regional loading stress is unable to generate dynamic rupture consistent with the observed faulting style. Resolving the regional tectonic stress field onto a single fault plane with a geometry as suggested by [Ellsworth et al. \(2019\)](#), [Korean Government Commission \(2019\)](#), and [Woo et al. \(2019\)](#), or onto the reconstructed **two fault planes**, leads **inevitable to pure strike-slip faulting**, in stark contrast to the observed thrust-faulting mechanism. Instead, local stress variation relative to regional stress orientation is needed to generate oblique faulting. **We conclude that regional-stress orientation may be misleading when assessing propensity for failure**, which in turn has important implications for seismic hazard assessment. Also, overpressurized pore fluids, nonoptimally oriented and dynamically weak faults, and a close to critical local stress state play major roles for our dynamic rupture models of the Pohang earthquake. Such factors may be assessed when planning and conducting EGS-type experiments, explorations, and operations.

Our dynamic rupture simulations reveal dynamic triggering from the main fault plane to the secondary fault plane without direct rupture branching but via “rupture jumping.” Model 2F simulation compares well with regional observed data such as moment release and far-field seismic waveforms. Model 1F, on the other hand, is unable to reproduce the observed non-DC focal mechanisms and surface displacement distributions due to simplicity of the dynamic rupture process and a shallower dip angle, respectively. Dynamic fault interaction, amplified by rapid stress changes due to seismic waves reverberating between the two fault planes, are needed to reproduce observations of a strong CLVD component. However, two simultaneously breaking fault planes cannot fully explain the observed source complexity.

We demonstrate the maturity and feasibility of high-resolution 3D modeling of rupture dynamics and seismic wave propagation, accounting for the complexity of EGS environments and constrained by few observational parameters shedding light on the dynamics of induced and triggered earthquakes. More sophisticated 3D models, fully coupling dynamic earthquake rupture and seismic wave propagation with coseismic and quasi-static fluid effects, such as **poroelasticity, thermal pressurization, pore pressure diffusion, and considering the geometric complexity of networks of fractures and nonplanar faults, will allow capturing the full physical complexity of nucleation and dynamics of induced earthquakes.**

In the near future, such physics-based approaches may be synergistically integrated with near-field seismic monitoring before, during, and after EGS operation, thus complementing traffic-light systems for hazard and risk mitigation ([Bommer et al., 2006](#); [Mignan et al., 2015](#)).

DATA AND RESOURCES

The open-source software package SeisSol can be downloaded in GitHub repository (<https://github.com/SeisSol/SeisSol>, last accessed July 2020). The procedure to download, compile, and execute the code is described in the documentation (<https://seissol.readthedocs.io/en/latest/>, last accessed July 2020). All regional waveforms used in this study were downloaded from Incorporated Research Institutions for Seismology (IRIS; <https://www.iris.edu>, last accessed June 2020) data management system using International Federation of Digital Seismograph Networks (FDSN) client. Preliminary reference Earth model (PREM) anisotropic 2 s can be downloaded in the IRIS data services products (<http://ds.iris.edu/ds/products/syngine/>, last accessed June 2020). The supplemental material for this article provides additional figures, a table, all parameters used for the preferred model 2F, mesh files, and a video mentioned in the article. All files required to reproduce the simulation can be accessed in Zenodo open-access repository (doi: [10.5281/zenodo.3930819](https://doi.org/10.5281/zenodo.3930819)).

ACKNOWLEDGMENTS

The authors thank Xing Li and Sigurjón Jónsson for the discussions regarding surface deformations using Interferometric Synthetic Aperture Radar (InSAR). The authors also thank Guy Ouillon for providing the raw code of anisotropic location uncertainty distribution (ACLDU). The authors acknowledge Seok Goo Song and Hoonyol Lee for sharing processed InSAR images and discussions about inversion parameters. The authors thank the Guest Editor, two anonymous reviewers, and Betty Schiefelbein for their insightful comments and constructive suggestions. Computing resources were provided by King Abdullah University of Science and Technology, Thuwal, Saudi Arabia (KAUST, Project k1219 and k1343 on Shaheen II). The work presented in this article was supported by KAUST Grants (FRacture Activation in Geo-reservoir-physics of induced Earthquakes in complex fault Networks [FRAGEN], URF/1/3389-01-01, and BAS/1339-01-01). Alice-Agnes Gabriel and Thomas Ulrich acknowledge support by the European Research Council European under the European Union’s Horizon 2020 research and innovation programme (Truly Extended Earthquake Rupture [TEAR], Grant Number 852992 and Centre of Excellence for Exascale in Solid Earth [ChEESE], Grant Number 823844) and the German Research Foundation (Deutsche Forschungsgemeinschaft [DFG]; Projects GA 2465/2-1, GA 2465/3-1) and by Kompetenznetzwerk für wissenschaftliches Höchstleistungsrechnen in Bayern (KONWIHR)—the Bavarian Competence Network for Technical and Scientific High Performance Computing (Project NewWave). José Ángel López-Comino has also received funding from the European Union’s Horizon 2020 research and innovation programme under the Marie Skłodowska-Curie Grant Agreement Number 754446 and Universidad de Granada (UGR) Research and Knowledge Transfer Found—Athenea3i; and by the DFG, German Research Foundation—Projektnummer (407141557). Part of the analysis was implemented using ObsPy ([Beyreuther et al., 2010](#)). Figures were prepared using Paraview ([Ahrens et al., 2005](#)), Generic Mapping Tools ([Wessel et al., 2013](#)), and Matplotlib ([Hunter, 2007](#)).

REFERENCES

- Ahrens, J., B. Geveci, and C. Law (2005). *ParaView: An End-User Tool for Large-Data Visualization*, Elsevier, 717–731.
Ando, R., and Y. Kaneko (2018). Dynamic rupture simulation reproduces spontaneous multifault rupture and arrest during the 2016

- M_w 7.9 Kaikoura earthquake, *Geophys. Res. Lett.* **45**, no. 23, 12,875–12,883, doi: [10.1029/2018GL080550](https://doi.org/10.1029/2018GL080550).
- Andrews, D. J. (2005). Rupture dynamics with energy loss outside the slip zone, *J. Geophys. Res.* **110**, no. B1, doi: [10.1029/2004JB003191](https://doi.org/10.1029/2004JB003191).
- Anger, S., and A.-A. Gabriel (2019). Dynamic earthquake rupture across complex 3D fracture networks, presented at the 2019 Fall Meeting, AGU, San Francisco, California, 9–13 December, S55E-0444.
- Aochi, H., and R. Madariaga (2003). The 1999 Izmit, Turkey, earthquake: Nonplanar fault structure, dynamic rupture process, and strong ground motion, *Bull. Seismol. Soc. Am.* **93**, no. 3, 1249–1266, doi: [10.1785/0120020167](https://doi.org/10.1785/0120020167).
- Aochi, H., O. Scotti, and C. Berge-Thierry (2005). Dynamic transfer of rupture across differently oriented segments in a complex 3-D fault system, *Geophys. Res. Lett.* **32**, no. 21, L21304, doi: [10.1029/2005GL024158](https://doi.org/10.1029/2005GL024158).
- Bauer, A., F. Scheipl, H. Küchenhoff, and A.-A. Gabriel (2018). An introduction to semiparametric function-on-scalar regression, *Stat. Model. Int. J.* **18**, nos. 3/4, 346–364, doi: [10.1177/1471082X17748034](https://doi.org/10.1177/1471082X17748034).
- Beyreuther, M., R. Barsch, L. Krischer, T. Megies, Y. Behr, and J. Wassermann (2010). ObsPy: A python toolbox for seismology, *Seismol. Res. Lett.* **81**, no. 3, 530–533, doi: [10.1785/gssrl.81.3.530](https://doi.org/10.1785/gssrl.81.3.530).
- Bhat, H. S., M. Olives, R. Dmowska, and J. R. Rice (2007). Role of fault branches in earthquake rupture dynamics, *J. Geophys. Res.* **112**, no. B11, doi: [10.1029/2007JB005027](https://doi.org/10.1029/2007JB005027).
- Boitz, N., A. Reshetnikov, and S. A. Shapiro (2018). Visualizing effects of anisotropy on seismic moments and their potency-tensor isotropic equivalent, *Geophysics* **83**, no. 3, C85–C97, doi: [10.1190/geo2017-0442.1](https://doi.org/10.1190/geo2017-0442.1).
- Bommer, J. J., S. Oates, J. M. Cepeda, C. Lindholm, J. Bird, R. Torres, G. Marroquín, and J. Rivas (2006). Control of hazard due to seismicity induced by a hot fractured rock geothermal project, *Eng. Geol.* **83**, no. 4, 287–306, doi: [10.1016/j.enggeo.2005.11.002](https://doi.org/10.1016/j.enggeo.2005.11.002).
- Breuer, A., A. Heinecke, and M. Bader (2016). Petascale local time stepping for the ADER-DG finite element method, *Proceedings – 2016 IEEE 30th International Parallel and Distributed Processing Symposium, IPDPS 2016*, Institute of Electrical and Electronics Engineers Inc., 854–863, doi: [10.1109/IPDPS.2016.109](https://doi.org/10.1109/IPDPS.2016.109).
- Breuer, A., A. Heinecke, S. Rettenberger, M. Bader, A.-A. Gabriel, and C. Pelties (2014). Sustained petascale performance of seismic simulations with SeisSol on SuperMUC, *International Supercomputing Conference*, Springer, Cham, doi: [10.1007/978-3-319-07518-1_1](https://doi.org/10.1007/978-3-319-07518-1_1).
- Buijze, L., P. A. J. van den Bogert, B. B. T. Wassing, B. Orlic, and J. Ten Veen (2017). Fault reactivation mechanisms and dynamic rupture modelling of depletion-induced seismic events in a Rotliegend gas reservoir, *Geol. Mijnbouw* **96**, no. 5, 131–148, doi: [10.1017/nmj.2017.27](https://doi.org/10.1017/nmj.2017.27).
- Bydlon, S. A., and E. M. Dunham (2015). Rupture dynamics and ground motions from earthquakes in 2-D heterogeneous media, *Geophys. Res. Lett.* **42**, no. 6, 1701–1709, doi: [10.1002/2014GL062982](https://doi.org/10.1002/2014GL062982).
- Caine, J. S., J. P. Evans, and C. B. Forster (1996). Fault zone architecture and permeability structure, *Geology* **24**, no. 11, 1025–1028, doi: [10.1130/0091-7613\(1996\)024<1025:fzaaps>2.3.co;2](https://doi.org/10.1130/0091-7613(1996)024<1025:fzaaps>2.3.co;2).
- Cappa, F., and J. Rutqvist (2012). Seismic rupture and ground accelerations induced by CO₂ injection in the shallow crust, *Geophys. J. Int.* **190**, no. 3, 1784–1789, doi: [10.1111/j.1365-246X.2012.05606.x](https://doi.org/10.1111/j.1365-246X.2012.05606.x).
- Chang, K. W., H. Yoon, Y. Kim, and M. Y. Lee (2020). Operational and geological controls of coupled poroelastic stressing and pore-pressure accumulation along faults: Induced earthquakes in Pohang, South Korea, *Sci. Rep.* **10**, no. 1, 2073, doi: [10.1038/s41598-020-58881-z](https://doi.org/10.1038/s41598-020-58881-z).
- Cheng, Y., and X. Chen (2018). Characteristics of seismicity inside and outside the Salton Sea geothermal field, *Bull. Seismol. Soc. Am.* **108**, no. 4, 1877–1888, doi: [10.1785/0120170311](https://doi.org/10.1785/0120170311).
- Cheng, Y., Z. E. Ross, and Y. Ben-Zion (2018). Diverse volumetric faulting patterns in the San Jacinto Fault Zone, *J. Geophys. Res.* **123**, no. 6, doi: [10.1029/2017JB015408](https://doi.org/10.1029/2017JB015408).
- Chester, F. M., J. P. Evans, and R. L. Biegel (1993). Internal structure and weakening mechanisms of the San Andreas fault, *J. Geophys. Res.* **98**, no. B1, 771–786, doi: [10.1029/92JB01866](https://doi.org/10.1029/92JB01866).
- Choi, J. H., K. Ko, Y. S. Gihn, C. S. Cho, H. Lee, S. G. Song, E. S. Bang, H. J. Lee, H. K. Bae, S. W. Kim, et al. (2019). Surface deformations and rupture processes associated with the 2017 M_w 5.4 Pohang, Korea, earthquake, *Bull. Seismol. Soc. Am.* **109**, no. 2, 756–769, doi: [10.1785/0120180167](https://doi.org/10.1785/0120180167).
- Cornet, F. H., T. Bérard, and S. Bourouis (2007). How close to failure is a granite rock mass at a 5 km depth? *Int. J. Rock. Mech. Min. Sci.* **44**, no. 1, 47–66, doi: [10.1016/j.ijrmms.2006.04.008](https://doi.org/10.1016/j.ijrmms.2006.04.008).
- Cuenot, N., J. Charléty, L. Dorbath, and H. Haessler (2006). Faulting mechanisms and stress regime at the European HDR site of Soultz-sous-Forêts, France, *Geothermics* **35**, nos. 5/6, 561–575, doi: [10.1016/j.geothermics.2006.11.007](https://doi.org/10.1016/j.geothermics.2006.11.007).
- de la Puente, J., J.-P. Ampuero, and M. Käser (2009). Dynamic rupture modeling on unstructured meshes using a discontinuous Galerkin method, *J. Geophys. Res.* **114**, no. B10, doi: [10.1029/2008JB006271](https://doi.org/10.1029/2008JB006271).
- Dieterich, J. H., K. B. Richards-Dinger, and K. A. Kroll (2015). Modeling injection-induced seismicity with the physics-based earthquake simulator RSQSim, *Seismol. Res. Lett.* **86**, no. 4, 1102–1109, doi: [10.1785/0220150057](https://doi.org/10.1785/0220150057).
- Di Toro, G., R. Han, T. Hirose, N. De Paola, S. Nielsen, K. Mizoguchi, F. Ferri, M. Cocco, and T. Shimamoto (2011). Fault lubrication during earthquakes, *Nature* **471**, no. 7339, 494–499, doi: [10.1038/nature09838](https://doi.org/10.1038/nature09838).
- Duan, B. (2016). Spontaneous rupture on natural fractures and seismic radiation during hydraulic fracturing treatments, *Geophys. Res. Lett.* **43**, no. 14, 7451–7458, doi: [10.1002/2016GL069083](https://doi.org/10.1002/2016GL069083).
- Dumbser, M., and M. Käser (2006). An arbitrary high-order discontinuous Galerkin method for elastic waves on unstructured meshes – II. The three-dimensional isotropic case, *Geophys. J. Int.* **167**, no. 1, 319–336, doi: [10.1111/j.1365-246X.2006.03120.x](https://doi.org/10.1111/j.1365-246X.2006.03120.x).
- Dunham, E. M., D. Belanger, L. Cong, and J. E. Kozdon (2011a). Earthquake ruptures with strongly rate-weakening friction and off-fault plasticity, part 1: Planar faults, *Bull. Seismol. Soc. Am.* **101**, no. 5, 2296–2307, doi: [10.1785/0120100075](https://doi.org/10.1785/0120100075).
- Dunham, E. M., D. Belanger, L. Cong, and J. E. Kozdon (2011b). Earthquake ruptures with strongly rate-weakening friction and off-fault plasticity, part 2: Nonplanar faults, *Bull. Seismol. Soc. Am.* **101**, no. 5, 2308–2322, doi: [10.1785/0120100076](https://doi.org/10.1785/0120100076).
- Ellsworth, W. L., D. Giardini, J. Townend, S. Ge, and T. Shimamoto (2019). Triggering of the Pohang, Korea, earthquake (M_w 5.5) by enhanced geothermal system stimulation, *Seismol. Res. Lett.* **90**, no. 5, 1844–1858, doi: [10.1785/0220190102](https://doi.org/10.1785/0220190102).
- Emerson Paradigm Holding (2019). *GoCad: A Computer Aided Design Program for Geological Applications*, Springer, Dordrecht, The Netherlands.

- Gabriel, A.-A., J.-P. Ampuero, L. A. Dalguer, and P. M. Mai (2012). The transition of dynamic rupture styles in elastic media under velocity-weakening friction, *J. Geophys. Res.* **117**, no. B9, doi: [10.1029/2012JB009468](https://doi.org/10.1029/2012JB009468).
- Gabriel, A.-A., J.-P. Ampuero, L. A. Dalguer, and P. M. Mai (2013). Source properties of dynamic rupture pulses with off-fault plasticity, *J. Geophys. Res.* **118**, no. 8, 4117–4126, doi: [10.1002/jgrb.50213](https://doi.org/10.1002/jgrb.50213).
- Gallos, M., J. P. Ampuero, P. M. Mai, and F. Cappa (2017). Induced seismicity provides insight into why earthquake ruptures stop, *Sci. Adv.* **3**, no. 12, doi: [10.1126/sciadv.aap7528](https://doi.org/10.1126/sciadv.aap7528).
- Gallovič, F., L. Valentová, J.-P. Ampuero, and A.-A. Gabriel (2019a). Bayesian dynamic finite-fault inversion: 1. Method and synthetic test, *J. Geophys. Res.* **124**, no. 7, 6949–6969, doi: [10.1029/2019JB017510](https://doi.org/10.1029/2019JB017510).
- Gallovič, F., L. Valentová, J.-P. Ampuero, and A.-A. Gabriel (2019b). Bayesian dynamic finite-fault inversion: 2. Application to the 2016 M_w 6.2 Amatrice, Italy, earthquake, *J. Geophys. Res.* **124**, no. 7, 6970–6988, doi: [10.1029/2019JB017512](https://doi.org/10.1029/2019JB017512).
- Garagash, D. I., and L. N. Germanovich (2012). Nucleation and arrest of dynamic slip on a pressurized fault, *J. Geophys. Res.* **117**, no. 10, doi: [10.1029/2012JB009209](https://doi.org/10.1029/2012JB009209).
- Grigoli, F., S. Cesca, A. P. Rinaldi, A. Manconi, J. A. López-Comino, J. F. Clinton, R. Westaway, C. Cauzzi, T. Dahm, and S. Wiemer (2018). The November 2017 M_w 5.5 Pohang earthquake: A possible case of induced seismicity in South Korea, *Science* **360**, no. 6392, 1003–1006, doi: [10.1126/science.aat2010](https://doi.org/10.1126/science.aat2010).
- Happ, C., F. Scheipl, A.-A. Gabriel, and S. Greven (2019). A general framework for multivariate functional principal component analysis of amplitude and phase variation, *Stat* **8**, no. 1, e220, doi: [10.1002/sta4.220](https://doi.org/10.1002/sta4.220).
- Hardebeck, J. L., and A. J. Michael (2006). Damped regional-scale stress inversions: Methodology and examples for southern California and the Coalinga aftershock sequence, *J. Geophys. Res.* **111**, no. B11, doi: [10.1029/2005JB004144](https://doi.org/10.1029/2005JB004144).
- Harris, R. A., M. Barall, B. Aagaard, S. Ma, D. Roten, K. Olsen, B. Duan, D. Lie, B. Luo, K. Bai, et al. (2018). A suite of exercises for verifying dynamic earthquake rupture codes, *Seismol. Res. Lett.* **89**, no. 3, 1146–1162, doi: [10.1785/0220170222](https://doi.org/10.1785/0220170222).
- Harris, R. A., M. Barall, D. J. Andrews, B. Duan, S. Ma, E. M. Dunham, A.-A. Gabriel, Y. Kaneko, Y. Kase, B. T. Aagaard, et al. (2011). Verifying a computational method for predicting extreme ground motion, *Seismol. Res. Lett.* **82**, no. 5, 638–644, doi: [10.1785/gssrl.82.5.638](https://doi.org/10.1785/gssrl.82.5.638).
- Heidbach, O., M. Rajabi, X. Cui, K. Fuchs, B. Muller, J. Reinecker, K. Reiter, M. Tingay, F. Wenzel, F. Xie, et al. (2018). The World Stress Map database release 2016: Crustal stress pattern across scales, *Tectonophysics* **744**, 484–498, doi: [10.1016/j.tecto.2018.07.007](https://doi.org/10.1016/j.tecto.2018.07.007).
- Heinecke, A., A. Breuer, S. Retenberger, M. Bader, A.-A. Gabriel, C. Pelties, A. Bode, W. Barth, X. Liao, K. Vaidyanathan, et al. (2014). Petascale high-order dynamic rupture earthquake simulations on heterogeneous supercomputers, *International Conf. for High Performance Computing, Networking, Storage and Analysis, SC*, IEEE Computer Society, 3–14, doi: [10.1109/SC.2014.6](https://doi.org/10.1109/SC.2014.6).
- Hillers, G., T. A. T. Vuorinen, M. R. Uski, J. T. Kortström, P. B. Mäntyniemi, T. Tiira, P. E. Malin, and T. Saarno (2020). The 2018 geothermal reservoir stimulation in Espoo/Helsinki, Southern Finland: Seismic network anatomy and data features, *Seismol. Res. Lett.* **91**, no. 2A, 770–786, doi: [10.1785/0220190253](https://doi.org/10.1785/0220190253).
- Hirata, T. (1989). Fractal dimension of fault systems in Japan: Fractal structure in rock fracture geometry at various scales, *Pure Appl. Geophys.* **131**, nos. 1/2, 157–170, doi: [10.1007/BF00874485](https://doi.org/10.1007/BF00874485).
- Hofmann, H., G. Zimmermann, M. Farkas, E. Huenges, A. Zang, M. Leonhardt, G. Kwiatek, P. Martinez-Garzon, M. Bohnhoff, K. B. Min, et al. (2019). First field application of cyclic soft stimulation at the Pohang Enhanced Geothermal System site in Korea, *Geophys. J. Int.* **217**, no. 2, 926–949, doi: [10.1093/gji/ggz058](https://doi.org/10.1093/gji/ggz058).
- Hunter, J. D. (2007). Matplotlib: A 2D graphics environment, *Comput. Sci. Eng.* **9**, no. 3, 99–104, doi: [10.1109/MCSE.2007.55](https://doi.org/10.1109/MCSE.2007.55).
- Jeanne, P., J. Rutqvist, P. F. Dobson, J. Garcia, M. Walters, C. Hartline, and A. Borgia (2015). Geomechanical simulation of the stress tensor rotation caused by injection of cold water in a deep geothermal reservoir, *J. Geophys. Res.* **120**, no. 12, 8422–8438, doi: [10.1002/2015JB012414](https://doi.org/10.1002/2015JB012414).
- Jin, L., and M. D. Zoback (2018). Fully dynamic spontaneous rupture due to quasi-static pore pressure and poroelastic effects: An implicit nonlinear computational model of fluid-induced seismic events, *J. Geophys. Res.* **123**, no. 11, 9430–9468, doi: [10.1029/2018JB015669](https://doi.org/10.1029/2018JB015669).
- Julian, B. R., A. D. Miller, and G. R. Foulger (1998). Non-double-couple earthquakes. 1. Theory, *Rev. Geophys.* **36**, no. 4, 525–549, doi: [10.1029/98RG00716](https://doi.org/10.1029/98RG00716).
- Kang, S., B. Kim, S. Bae, H. Lee, and M. Kim (2019). Earthquake-induced ground deformations in the low-seismicity region: A case of the 2017 M5.4 Pohang, South Korea, earthquake, *Earthq. Spectra* **35**, no. 3, 1235–1260, doi: [10.1193/062318EQS160M](https://doi.org/10.1193/062318EQS160M).
- Kang, S., B. Kim, H. Cho, J. Lee, K. Kim, S. Bae, and C. Sun (2019). Ground-motion amplifications in small-size hills: Case study of Gokgang-Ri, South Korea, during the 2017 M_L 5.4 Pohang earthquake sequence, *Bull. Seismol. Soc. Am.* **109**, no. 6, 2626–2643, doi: [10.1785/0120190064](https://doi.org/10.1785/0120190064).
- Käser, M., and M. Dumbser (2006). An arbitrary high-order discontinuous Galerkin method for elastic waves on unstructured meshes—I. The two-dimensional isotropic case with external source terms, *Geophys. J. Int.* **166**, no. 2, 855–877, doi: [10.1111/j.1365-246X.2006.03051.x](https://doi.org/10.1111/j.1365-246X.2006.03051.x).
- Kim, H., L. Xie, K. B. Min, S. Bae, and O. Stephansson (2017). Integrated in situ stress estimation by hydraulic fracturing, borehole observations and numerical analysis at the EXP-1 borehole in Pohang, Korea, *Rock Mech. Rock Eng.* **50**, no. 12, 3141–3155, doi: [10.1007/s00060-017-1284-1](https://doi.org/10.1007/s00060-017-1284-1).
- Kim, K. H., J. H. Ree, Y. H. Kim, S. Kim, S. Y. Kang, and W. Seo (2018). Assessing whether the 2017 M_w 5.4 Pohang earthquake in South Korea was an induced event, *Science* **360**, no. 6392, 1007–1009, doi: [10.1126/science.aat0801](https://doi.org/10.1126/science.aat0801).
- Kim, K. H., W. Seo, J. Han, J. Kwon, S. Y. Kang, J. H. Ree, S. Kim, and K. Liu (2020). The 2017 M_L 5.4 Pohang earthquake sequence, Korea, recorded by a dense seismic network, *Tectonophysics* **774**, doi: [10.1016/j.tecto.2019.228306](https://doi.org/10.1016/j.tecto.2019.228306).
- Klinger, Y., K. Okubo, A. Vallage, J. Champenois, A. Delorme, E. Rougier, Z. Lei, E. E. Knight, A. Munjiza, C. Satriano, et al. (2018). Earthquake damage patterns resolve complex rupture processes, *Geophys. Res. Lett.* **45**, no. 19, 10,279–10,287, doi: [10.1029/2018GL078842](https://doi.org/10.1029/2018GL078842).
- Korean Government Commission (2019). *Summary Report of the Korean Government Commission on Relations between the 2017*

- Pohang Earthquake and EGS Project*, Geological Society of Korea, Seoul, South Korea, doi: [10.22719/KETEP-20183010111860](https://doi.org/10.22719/KETEP-20183010111860).
- Krischer, L., A. R. Hutko, M. Van Driel, S. Stähler, M. Bahavar, C. Trabant, and T. Nissen-Meyer (2017). On-demand custom broadband synthetic seismograms, *Seismol. Res. Lett.* **88**, no. 4, 1127–1140, doi: [10.1785/0220160210](https://doi.org/10.1785/0220160210).
- Kroll, K. A., K. B. Richards-Dinger, and J. H. Dieterich (2017). Sensitivity of induced seismic sequences to rate-and-state frictional processes, *J. Geophys. Res.* **122**, no. 12, 10,207–10,219, doi: [10.1002/2017JB014841](https://doi.org/10.1002/2017JB014841).
- Kwiatek, G., T. Saarno, T. Ader, F. Bluemle, M. Bohnhoff, M. Chendorain, G. Dresen, P. Heikkinen, I. Kukkonen, P. Leary, et al. (2019). Controlling fluid-induced seismicity during a 6.1-km-deep geothermal stimulation in Finland, *Sci. Adv.* **5**, no. 5, eaav7224, doi: [10.1126/sciadv.aav7224](https://doi.org/10.1126/sciadv.aav7224).
- Kyriakopoulos, C., D. D. Oglesby, T. K. Rockwell, A. J. Meltzner, M. Barall, J. M. Fletcher, and D. Tulanowski (2019). Dynamic rupture scenarios in the Brawley Seismic Zone, Salton Trough, Southern California, *J. Geophys. Res.* **124**, no. 4, 3680–3707, doi: [10.1029/2018JB016795](https://doi.org/10.1029/2018JB016795).
- Lee, H., Y. J. Shinn, S. H. Ong, S. W. Woo, K. G. Park, T. J. Lee, and S. W. Moon (2017). Fault reactivation potential of an offshore CO₂ storage site, Pohang Basin, South Korea, *J. Pet. Sci. Eng.* **152**, 427–442, doi: [10.1016/j.petrol.2017.03.014](https://doi.org/10.1016/j.petrol.2017.03.014).
- Lee, J., T. K. Hong, and C. Chang (2017). Crustal stress field perturbations in the continental margin around the Korean Peninsula and Japanese islands, *Tectonophysics* **718**, 140–149, doi: [10.1016/j.tecto.2017.08.003](https://doi.org/10.1016/j.tecto.2017.08.003).
- Lee, K. K., W. L. Ellsworth, D. Giardini, J. Townend, S. Ge, T. Shimamoto, I. W. Yeo, T. S. Kang, J. Rhie, D. G. Sheen, et al. (2019). Managing injection-induced seismic risks, *Science* **364**, no. 6442, 730–732, doi: [10.1126/science.aax1878](https://doi.org/10.1126/science.aax1878).
- Lim, H., K. Deng, Y. H. Kim, J.-H. Ree, T.-R. A. Song, and K.-H. Kim (2020). The 2017 M_w 5.5 Pohang earthquake, South Korea, and poroelastic stress changes associated with fluid injection, *J. Geophys. Res.* **125**, doi: [10.1029/2019jb019134](https://doi.org/10.1029/2019jb019134).
- Liu, J., and J. Zahradník (2020). The 2019 M_w 5.7 Changning earthquake, Sichuan Basin, China. A shallow doublet with different faulting styles, *Geophys. Res. Lett.* **47**, no. 4, 1–2, doi: [10.1029/2019GL085408](https://doi.org/10.1029/2019GL085408).
- Ma, S. (2008). A physical model for widespread near-surface and fault zone damage induced by earthquakes, *Geochem. Geophys. Geosys.* **9**, no. 11, doi: [10.1029/2008GC002231](https://doi.org/10.1029/2008GC002231).
- Mai, P. M., M. Galis, K. K. S. Thingbaijam, J. C. Vyas, and E. M. Dunham (2018). Accounting for fault roughness in pseudo-dynamic ground-motion simulations, *Pure Appl. Geophys.* **174**, 3419–3450, doi: [10.1007/s00024-017-1536-8](https://doi.org/10.1007/s00024-017-1536-8).
- Martínez-Garzón, P., M. Bohnhoff, G. Kwiatek, and G. Dresen (2013). Stress tensor changes related to fluid injection at The Geysers geothermal field, California, *Geophys. Res. Lett.* **40**, no. 11, 2596–2601, doi: [10.1002/grl.50438](https://doi.org/10.1002/grl.50438).
- Martínez-Garzón, P., G. Kwiatek, H. Sone, M. Bohnhoff, G. Dresen, and C. Hartline (2014). Spatiotemporal changes, faulting regimes, and source parameters of induced seismicity: A case study from The Geysers geothermal field, *J. Geophys. Res.* **119**, no. 11, 8378–8396, doi: [10.1002/2014JB011385](https://doi.org/10.1002/2014JB011385).
- McGarr, A. (2014). Maximum magnitude earthquakes induced by fluid injection, *J. Geophys. Res.* **119**, no. 2, 1008–1019, doi: [10.1002/2013JB010597](https://doi.org/10.1002/2013JB010597).
- Mignan, A., D. Landtwing, P. Kästli, B. Mena, and S. Wiemer (2015). Induced seismicity risk analysis of the 2006 Basel, Switzerland, Enhanced Geothermal System project: Influence of uncertainties on risk mitigation, *Geothermics* **53**, 133–146, doi: [10.1016/j.geothermics.2014.05.007](https://doi.org/10.1016/j.geothermics.2014.05.007).
- Mitchell, T. M., and D. R. Faulkner (2009). The nature and origin of off-fault damage surrounding strike-slip fault zones with a wide range of displacements: A field study from the Atacama fault system, northern Chile, *J. Struct. Geol.* **31**, no. 8, doi: [10.1016/j.jsg.2009.05.002](https://doi.org/10.1016/j.jsg.2009.05.002).
- Okubo, K., H. S. Bhat, E. Rougier, S. Marty, A. Schubnel, Z. Lei, E. E. Knight, and Y. Klinger (2019). Dynamics, radiation, and overall energy budget of earthquake rupture with coseismic off-fault damage, *J. Geophys. Res.* **124**, no. 11, 11,771–11,801, doi: [10.1029/2019JB017304](https://doi.org/10.1029/2019JB017304).
- Pelties, C., J. de la Puente, J.-P. Ampuero, G. B. Brietzke, and M. Käser (2012). Three-dimensional dynamic rupture simulation with a high-order discontinuous Galerkin method on unstructured tetrahedral meshes, *J. Geophys. Res.* **117**, no. B2, doi: [10.1029/2011JB008857](https://doi.org/10.1029/2011JB008857).
- Pelties, C., A.-A. Gabriel, and J.-P. Ampuero (2014). Verification of an ADER-DG method for complex dynamic rupture problems, *Geosci. Model Dev.* **7**, no. 3, 847–866, doi: [10.5194/gmd-7-847-2014](https://doi.org/10.5194/gmd-7-847-2014).
- Pelties, C., Y. Huang, and J.-P. Ampuero (2015). Pulse-like rupture induced by three-dimensional fault zone flower structures, *Pure Appl. Geophys.* **172**, no. 5, 1229–1241, doi: [10.1007/s00024-014-0881-0](https://doi.org/10.1007/s00024-014-0881-0).
- Peyrat, S., K. Olsen, and R. Madariaga (2001). Dynamic modeling of the 1992 Landers earthquake, *J. Geophys. Res.* **106**, no. B11, 26,467–26,482, doi: [10.1029/2001jb000205](https://doi.org/10.1029/2001jb000205).
- Rettenberger, S., O. Meister, M. Bader, and A.-A. Gabriel (2016). ASAGI—A parallel server for adaptive geoinformation, *EASC '16: Proc. of the Exascale Applications and Software Conference 2016*, April 2016, Article Number 2, 1–9, doi: [10.1145/2938615.2938618](https://doi.org/10.1145/2938615.2938618).
- Richards-Dinger, K., and J. H. Dieterich (2012). RSQSim earthquake simulator, *Seismol. Res. Lett.* **83**, no. 6, 983–990, doi: [10.1785/0220120105](https://doi.org/10.1785/0220120105).
- Ripperger, J., P. M. Mai, and J.-P. Ampuero (2008). Variability of near-field ground motion from dynamic earthquake rupture simulations, *Bull. Seismol. Soc. Am.* **98**, no. 3, 1207–1228, doi: [10.1785/0120070076](https://doi.org/10.1785/0120070076).
- Ross, Z. E., B. Idini, Z. Jia, O. L. Stephenson, M. Zhong, X. Wang, Z. Zhan, M. Simons, E. J. Fielding, S. H. Yun, et al. (2019). Hierarchical interlocked orthogonal faulting in the 2019 Ridgecrest earthquake sequence, *Science* **366**, no. 6463, 346–351, doi: [10.1126/science.aaz0109](https://doi.org/10.1126/science.aaz0109).
- Roten, D., K. B. Olsen, S. M. Day, Y. Cui, and D. Fäh (2014). Expected seismic shaking in Los Angeles reduced by San Andreas fault zone plasticity, *Geophys. Res. Lett.* **41**, no. 8, 2769–2777, doi: [10.1002/2014GL059411](https://doi.org/10.1002/2014GL059411).
- Schoenball, M., L. Dorbath, E. Gaucher, J. F. Wellmann, and T. Kohl (2014). Change of stress regime during geothermal reservoir stimulation, *Geophys. Res. Lett.* **41**, no. 4, 1163–1170, doi: [10.1002/2013GL058514](https://doi.org/10.1002/2013GL058514).
- Schoenball, M., T. M. Müller, B. I. R. Müller, and O. Heidbach (2010). Fluid-induced microseismicity in pre-stressed rock masses, *Geophys. J. Int.* **180**, no. 2, 813–819, doi: [10.1111/j.1365-246X.2009.04443.x](https://doi.org/10.1111/j.1365-246X.2009.04443.x).

- Shi, Z., and S. M. Day (2013). Rupture dynamics and ground motion from 3-D rough-fault simulations, *J. Geophys. Res.* **118**, no. 3, 1122–1141, doi: [10.1002/jgrb.50094](https://doi.org/10.1002/jgrb.50094).
- Simmetrix Inc. (2019). SimModeler: Simulation modeling suite 14.0 documentation, *Tech. Report*.
- Soh, I., C. Chang, J. Lee, T.-K. Hong, and E.-S. Park (2018). Tectonic stress orientations and magnitudes, and friction of faults, deduced from earthquake focal mechanism inversions over the Korean Peninsula, *Geophys. J. Int.* **213**, no. 2, 1360–1373, doi: [10.1093/gji/ggy061](https://doi.org/10.1093/gji/ggy061).
- Song, S. G., and H. Lee (2019). Static slip model of the 2017 M_w 5.4 Pohang, South Korea, earthquake constrained by the InSAR data, *Seismol. Res. Lett.* **90**, no. 1, 140–148, doi: [10.1785/0220180156](https://doi.org/10.1785/0220180156).
- Taufiqurrahman, T., A.-A. Gabriel, B. Li, D. Li, S. A. Wirp, T. Ulrich, K. H. Palgunadi, A. Verdecchia, S. Carena, and Z. K. Mildon (2019). High-resolution integrated dynamic rupture modeling of the 2019 M6.4 Searles Valley and M7.1 Ridgecrest earthquakes, presented at the 2019 Fall Meeting, AGU, San Francisco, California, 9–13 December, S31G-0487.
- Templeton, E. L., and J. R. Rice (2008). Off-fault plasticity and earthquake rupture dynamics: 1. Dry materials or neglect of fluid pressure changes, *J. Geophys. Res.* **113**, no. B9, doi: [10.1029/2007JB005529](https://doi.org/10.1029/2007JB005529).
- Ulrich, T., A.-A. Gabriel, J.-P. Ampuero, and W. Xu (2019). Dynamic viability of the 2016 M_w 7.8 Kaikōura earthquake cascade on weak crustal faults, *Nat. Comm.* **10**, no. 1, doi: [10.1038/s41467-019-10912-w](https://doi.org/10.1038/s41467-019-10912-w).
- Ulrich, T., A.-A. Gabriel, and C. Uphoff (2019). Are multi-fault rupture and fault roughness compatible? Dynamic rupture modeling of the 2016 Kaikōura, New Zealand, rupture cascade with geometric fault complexity across scales, presented at the 2019 Fall Meeting, AGU, San Francisco, California, 9–13 December, S51E-0432U.
- Ulrich, T., S. Vater, E. H. Madden, J. Behrens, Y. van Dinther, I. van Zelst, E. J. Fielding, C. Liang, and A.-A. Gabriel (2019). Coupled, physics-based modeling reveals earthquake displacements are critical to the 2018 Palu, Sulawesi Tsunami, *Pure Appl. Geophys.* **176**, no. 10, 4069–4109, doi: [10.1007/s00024-019-02290-5](https://doi.org/10.1007/s00024-019-02290-5).
- Uphoff, C., and M. Bader (2016). Generating high performance matrix kernels for earthquake simulations with viscoelastic attenuation, *2016 International Conf. on High Performance Computing and Simulation (HPCS), IEEE*, 908–916, doi: [10.1109/HPCSim.2016.7568431](https://doi.org/10.1109/HPCSim.2016.7568431).
- Uphoff, C., S. Rettenberger, M. Bader, E. H. Madden, T. Ulrich, S. Wollherr, and A.-A. Gabriel (2017). Extreme scale multi-physics simulations of the tsunamigenic 2004 Sumatra megathrust earthquake, *Proc. Int. Conf. High Perform. Comput. Networking, Storage Anal.—SC ’17*, November, 1–16, doi: [10.1145/3126908.3126948](https://doi.org/10.1145/3126908.3126948).
- van Zelst, I., S. Wollherr, A.-A. Gabriel, E. H. Madden, and Y. van Dinther (2019). Modeling megathrust earthquakes across scales: One-way coupling from geodynamics and seismic cycles to dynamic rupture, *J. Geophys. Res.* **124**, no. 11, 11,414–11,446, doi: [10.1029/2019JB017539](https://doi.org/10.1029/2019JB017539).
- Vavryčuk, V. (2015). Moment tensor decompositions revisited, *J. Seismol.* **19**, no. 1, 231–252, doi: [10.1007/s10950-014-9463-y](https://doi.org/10.1007/s10950-014-9463-y).
- Viesca, R. C., and J. R. Rice (2012). Nucleation of slip-weakening rupture instability in landslides by localized increase of pore pressure, *J. Geophys. Res.* **117**, no. 3, doi: [10.1029/2011JB008866](https://doi.org/10.1029/2011JB008866).
- Wang, Y., G. Ouillon, J. Woessner, D. Sornette, and S. Husen (2013). Automatic reconstruction of fault networks from seismicity catalogs including location uncertainty, *J. Geophys. Res.* **118**, no. 11, 5956–5975, doi: [10.1002/2013JB010164](https://doi.org/10.1002/2013JB010164).
- Wessel, P., W. H. F. Smith, R. Scharroo, J. Luis, and F. Wobbe (2013). Generic Mapping Tools: Improved version released, *Eos Trans. AGU* **94**, no. 45, 409–410, doi: [10.1002/2013EO450001](https://doi.org/10.1002/2013EO450001).
- Wolf, S., A.-A. Gabriel, and M. Bader (2020). Optimisation and local time stepping of an ADER-DG scheme for fully anisotropic wave propagation in complex geometries, in V. V. Krzhizhanovskaya, G. Závodszky, M. H. Lees, J. J. Dongarra, P. M. A. Sloot, S. Brissos, and J. Teixeira (Editors), *Proc. of the 10th International Workshop on Advances in High-Performance Computational Earth Sciences: Applications and Frameworks, Computer Science—ICCS 2020: ICCS 2020*, Lecture Notes in Computer Science 12139, 32–45, doi: [10.1007/978-3-030-50420-5_3](https://doi.org/10.1007/978-3-030-50420-5_3).
- Wollherr, S., A.-A. Gabriel, and P. M. Mai (2019). Landers 1992 “Reloaded”: Integrative dynamic earthquake rupture modeling, *J. Geophys. Res.* **124**, no. 7, 6666–6702, doi: [10.1029/2018JB016355](https://doi.org/10.1029/2018JB016355).
- Wollherr, S., A.-A. Gabriel, and C. Uphoff (2018). Off-fault plasticity in three-dimensional dynamic rupture simulations using a modal discontinuous Galerkin method on unstructured meshes: Implementation, verification and application, *Geophys. J. Int.* **214**, no. 3, 1556–1584, doi: [10.1093/GJI/GGY213](https://doi.org/10.1093/GJI/GGY213).
- Woo, J.-U., M. Kim, D.-H. Sheen, T.-S. Kang, J. Rhie, F. Grigoli, W. L. Ellsworth, and D. Giardini (2019). An in-depth seismological analysis revealing a causal link between the 2017 M_w 5.5 Pohang earthquake and EGS project, *J. Geophys. Res.* **124**, no. 12, doi: [10.1029/2019JB018368](https://doi.org/10.1029/2019JB018368).
- Yamashita, T., and Y. Umeda (1994). Earthquake rupture complexity due to dynamic nucleation and interaction of subsidiary faults, *Pure Appl. Geophys.* **143**, nos. 1/3, 89–116, doi: [10.1007/BF00874325](https://doi.org/10.1007/BF00874325).
- Zaliapin, I., and Y. Ben-Zion (2013). Earthquake clusters in southern California I: Identification and stability, *J. Geophys. Res.* **118**, no. 6, 2847–2864, doi: [10.1002/jgrb.50179](https://doi.org/10.1002/jgrb.50179).
- Zhan, Z. (2019). Distributed acoustic sensing turns fiber-optic cables into sensitive seismic antennas, *Seismol. Res. Lett.* **91**, no. 1, 1–15, doi: [10.1785/0220190112](https://doi.org/10.1785/0220190112).
- Zhang, Q., and P. M. Shearer (2016). A new method to identify earthquake swarms applied to seismicity near the San Jacinto Fault, California, *Geophys. J. Int.* **205**, no. 2, 995–1005, doi: [10.1093/gji/ggw073](https://doi.org/10.1093/gji/ggw073).
- Ziegler, M. O., O. Heidbach, A. Zang, P. Martínez-Garzón, and M. Bohnhoff (2017). Estimation of the differential stress from the stress rotation angle in low permeable rock, *Geophys. Res. Lett.* **44**, no. 13, 6761–6770, doi: [10.1002/2017GL073598](https://doi.org/10.1002/2017GL073598).

APPENDIX

Friction parameters

To parameterize the frictional behavior, we use laboratory-based rapid velocity weakening friction law proposed by the community benchmark problem TPV104 Southern California Earthquake Center (SCEC-benchmark) (Harris *et al.*, 2018). The friction law is adapted from the formulation introduced by Dunham *et al.* (2011a). The governing equations in our notation are described in Ulrich, Gabriel, Ampuero, and Xu (2019);

the implementation in SeisSol (see [Data and Resources](#)) is described and verified in [Pelties et al. \(2014\)](#). Figure S1b shows the depth-dependent direct effect a and weakening slip velocity V_W . The evolution effect parameter b is set constant. We apply a velocity strengthening zone at the top 200 m of all faults to smoothly stop rupture. Within this zone, values for a and V_W increase linearly ranging from 0.01 and 0.1 m/s below depth of 3.3 km to 0.02 and 1.0 m/s to the surface, respectively. Table A1 lists all friction parameters used in this study.

Nucleation procedure

To nucleate the earthquake, we apply a time-dependent overstress centered at the hypocenter location that is at longitude and latitude of 129.37° and 36.11°, respectively, and at a depth of 4.27 km. The time-dependent overstressed nucleation area $R_{\text{nuc}}(t)$ is determined by increasing the initial relative prestress ratio R_0 as

$$R_{\text{nuc}}(t) = R_0 + \Omega(r) \times S(t), \quad (\text{A1})$$

in which $\Omega(r)$ is a Gaussian-step function, r is the radius from the hypocenter, and $S(t)$ denotes the smoothed step function. The Gaussian-step function is defined as

$$\begin{aligned} \Omega(r) &= \xi \exp\left(\frac{r^2}{r_c^2 - r^2}\right) \quad \text{for } r < r_c; \\ \Omega(r) &= 0 \quad \text{otherwise,} \end{aligned} \quad (\text{A2})$$

in which ξ is the overstressed initial relative prestress ratio and $r_c = 500$ m is the radius of the nucleation patch. We only overstress the main fault plane; in the nucleation region, we set ξ to 2, and apply an overstress characterized by $S_{\text{Hmax}} = 77^\circ$ and $v = 0.1$. These values are set by trial-and-error to allow rupture to propagate spontaneously with the least magnitude of overstress and to limit fault slip inside the nucleation patch. The orientation of S_{Hmax} is also in accordance with [Korean Government Commission \(2019\)](#) and [Ellsworth et al. \(2019\)](#), which suggest optimally oriented stress orientation and critically stressed inside the nucleation zone. The smoothed step function is formulated as

$$S(t) = \text{Exp}\left(\frac{(t-T)^2}{t \times (t-2 \times T)}\right) \quad \text{for } 0 < t < T; \quad S(t) = 1 \quad \text{for } t \geq T, \quad (\text{A3})$$

in which $T = 0.4$ s is the nucleation time.

Numerical method

We use the open-source software SeisSol ([Dumbser and Käser, 2006](#); [Pelties et al., 2014](#); [Uphoff et al., 2017](#); [Wollherr et al., 2018](#); see [Data and Resources](#)), which couples seismic wave propagation in complex media and frictional fault failure. SeisSol uses an Arbitrary high-order DERivative-Discontinuous Galerkin (ADER-DG) approach, which achieves high-order accuracy in

space and time ([Käser and Dumbser, 2006](#)). SeisSol uses flexible nonuniform unstructured tetrahedral mesh, which allows accounting for complex geometric features such as 3D fault networks or high-resolution topography across a large range of scales: from small-scale fault roughness, large-scale fault structures, to fault-to-fault interaction. Dynamic rupture simulations are sensitive to geometrically complexity of faults ([Dunham et al., 2011b](#); [Shi and Day, 2013](#); [Uphoff et al., 2017](#); [Wollherr et al., 2018, 2019](#); [Ulrich, Gabriel, Ampuero, and Xu, 2019](#); [Ulrich, Vater, et al., 2019](#)).

High resolution and accurate simulations are essential to resolve the detailed processes of rupture propagation of the intersected fault geometry. We motivate the presented deterministic parameter study with the computational feasibility of many such simulations. Although the feasibility of dynamic rupture inversion and statistical learning approaches has been demonstrated (e.g., [Peyrat et al., 2001](#); [Bauer et al., 2018](#); [Gallovič et al., 2019a,b](#); [Happ et al., 2019](#)), these are restricted by near-field data availability and the computational cost of each forward dynamic rupture model.

SeisSol is verified in a wide range of benchmark problems, including dipping faults, branched and curved faults, on-fault heterogeneity, and laboratory-based friction laws ([de la Puente et al., 2009](#); [Pelties et al., 2012, 2014](#); [Wollherr et al., 2018](#)) in line with the SCEC-Benchmark Dynamic Rupture code verification exercises ([Harris et al., 2011](#); [Harris et al., 2018](#)) as well as against analytical reference solutions for seismic wave propagation (e.g., [Uphoff and Bader, 2016](#); [Wolf et al., 2020](#)). Fast time to solution is achieved using end-to-end optimization ([Breuer et al., 2014](#); [Heinecke et al., 2014](#); [Rettenberger et al., 2016](#)), including an efficient local time-stepping algorithm ([Breuer et al., 2016](#); [Uphoff et al., 2017](#)). This efficient algorithm on high-performance computing architecture provides up to 10-fold speed up ([Uphoff et al., 2017](#)).

SeisSol allows accounting for off-fault yielding. Inelastic energy dissipation influences rupture dynamics such as rupture speed and rupture style (e.g., [Gabriel et al., 2013](#)). Off-fault

TABLE A1
Fault Friction Parameters Assumed in This Study

Parameter	Symbol	Value
Direct effect parameter	a	0.01–0.02 $z \leq 3.3$ km and 0.01 $z > 3.3$ km
Evolution effect parameter	b	0.014
Reference slip velocity	V_0	10^{-6} m/s
Steady-state friction coefficient at V_0	f_0	0.6
State-evolution distance	L	0.2 m
Weakening slip velocity	V_W	0.1–1.0 $z \leq 3.3$ km and 0.1 $z > 3.3$ km
Fully weakened friction coefficient	f_W	0.1
Initial slip rate	V_{ini}	10^{-16} m/s

plasticity is incorporated using the off-line code generator to compute matrix operations in an efficient way (Wollherr *et al.*, 2018). SeisSol also supports viscoelastic rheologies, using an off-line code generator similar to that of off-fault plasticity. In this study, we use a spatiotemporal discretization of polynomial degree $p = 4$ (O5) for all simulations.

Mesh generation

The simulation domain and fault-plane geometry model are created using third-party software GoCad (Emerson Paradigm Holding, 2019) in a Cartesian coordinate system. We discretize the unstructured tetrahedral mesh using the meshing software Simmodeler (Simmetrix Inc., 2019). The mesh element edge length is 50 m close to the fault plane and 200 m at the surface topography, yielding a 4 million volume cell mesh. The mesh size on the fault plane is examined prior to the simulation by calculating the cohesive zone (or process zone) to ensure convergence. Wollherr *et al.* (2018) provide a way to resolve the cohesive zone for the case of SeisSol. To save the computational costs and at the same time avoid reflections from the domain boundary, we gradually increase the edge length size of the

tetrahedral element by a factor of 6% away from the fault plane and surface topography. Figure 3 depicts the unstructured tetrahedral mesh used in this study, overlain by a snapshot of the absolute velocity field at simulation time $t = 5$ s, for our preferred dynamic rupture model (model 2F), highlighting the effect of topography on near-field ground motions.

The locally refined mesh and high-order spatiotemporal discretization allow capturing the high-frequency content of the waveforms with high accuracy (minimal numerical dispersion), especially in the near-fault region. We estimate that the maximum resolved frequency is up to 4 Hz within 7 km distance from the fault zone and around 1 Hz at 30 km distance from the fault. Simulating 5 s typically requires 15 min (average runtime) on Intel Haswell cores with 128 nodes using supercomputer Cray XC40 Shaheen-II, King Abdullah University of Science and Technology, Saudi Arabia.

Manuscript received 4 March 2020

Published online 4 August 2020